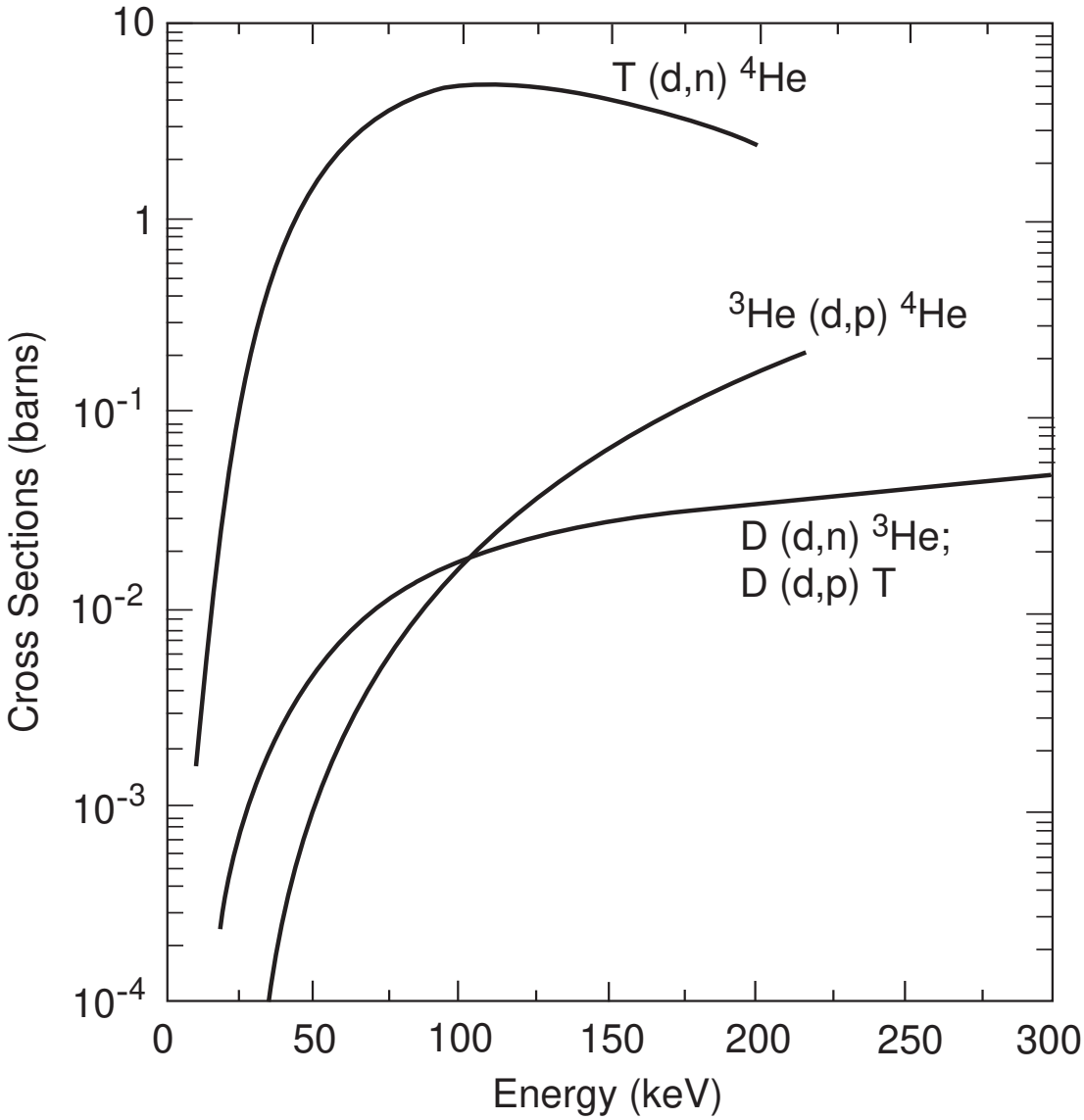

Fig. 1 Cross sections for fusion reactions of importance in magnetic fusion are plotted versus energy.

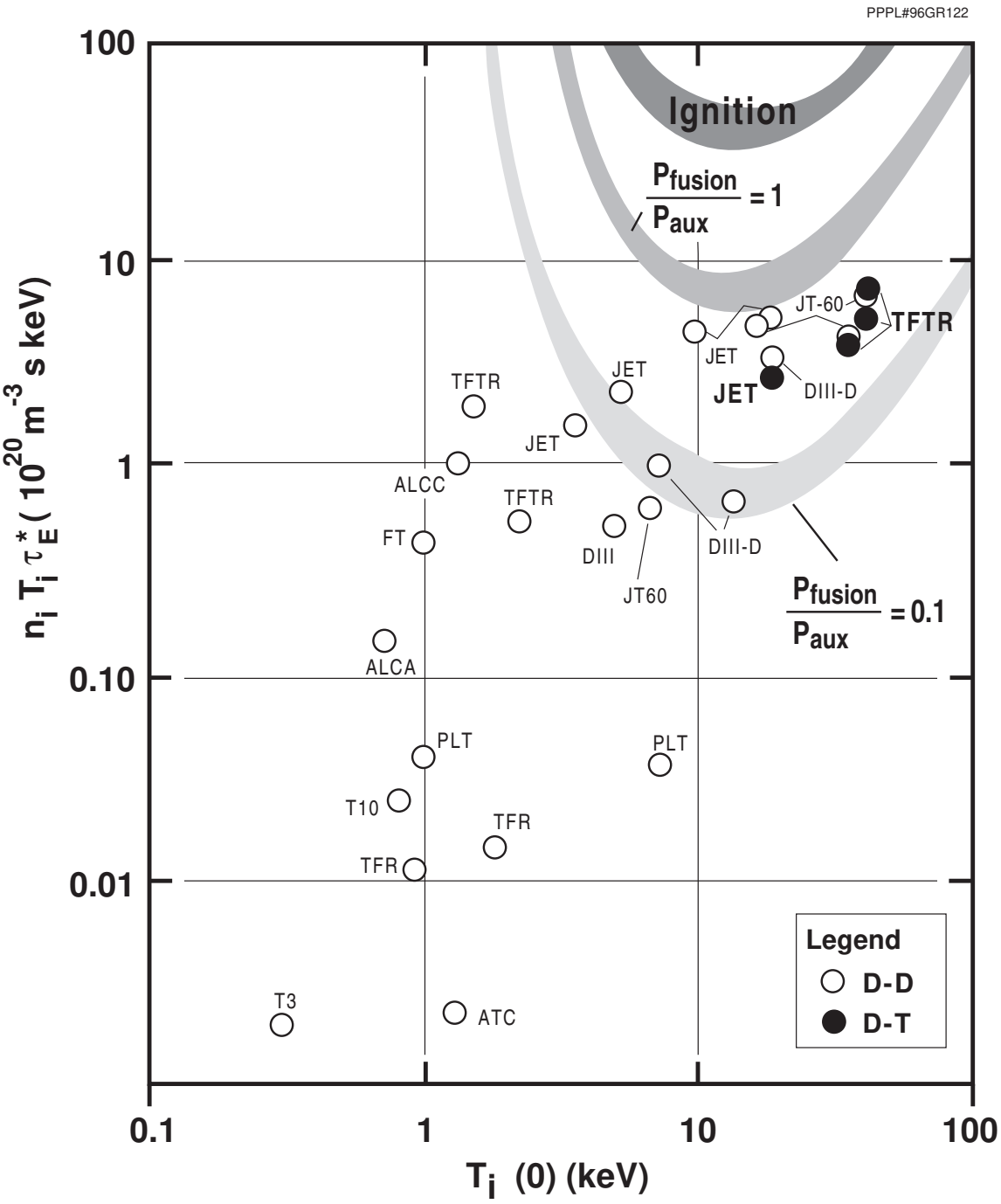

Fig. 2 The achieved product $n_{HYD}\ T_i(0)\ \tau_E^*$ where n_{HYD} is the sum of all hydrogenic densities versus $T_i(0)$ for various tokamak devices. In present devices, P_{breh} is small compared with P_{aux} and ignored. For comparison, an estimate of the criteria for $P_{fus}/P_{aux} = 1$ and ignition in which the alpha heating sustains the plasma is given.

Fig. 3 The interior of the TFTR vacuum vessel is shown. The carbon-composite and graphite tiles on the inner wall limits the plasma and protects the vacuum vessel wall.

Fig. 4 Interior of the JET vacuum vessel (JET Team, 1992).

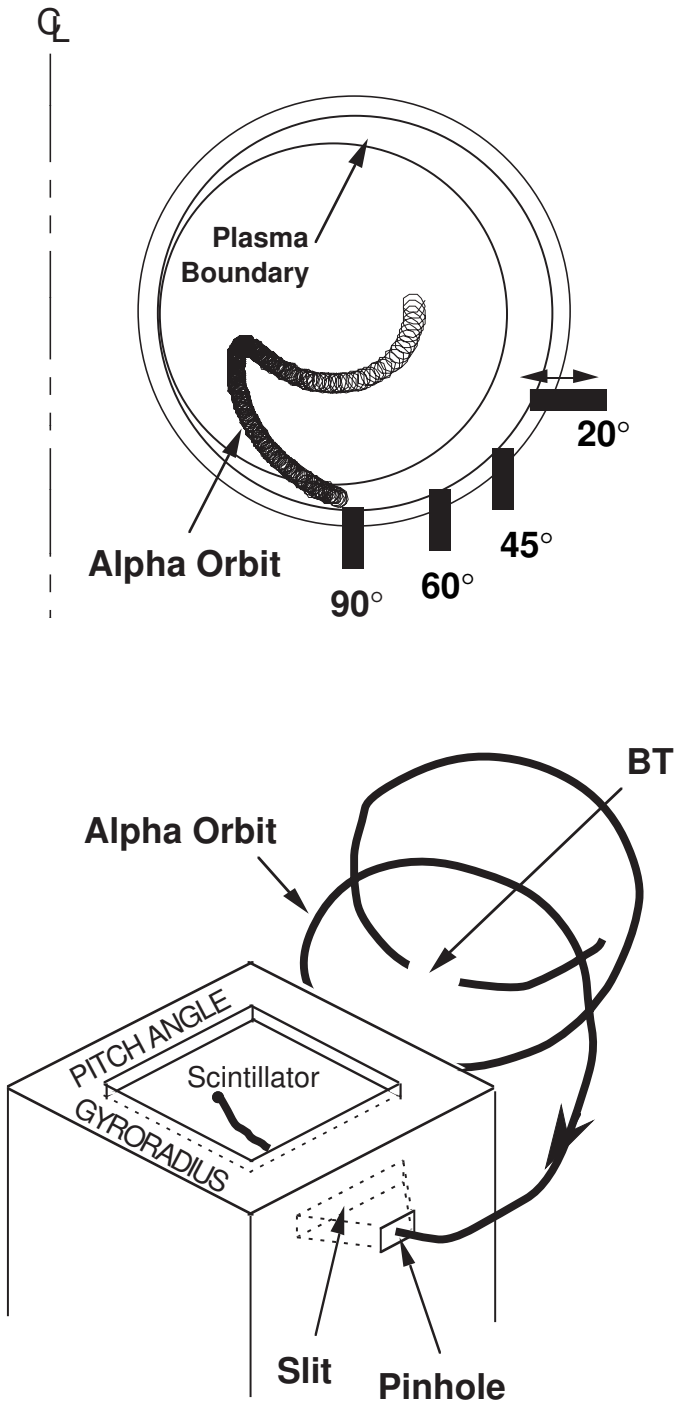

Fig. 5 Four lost alpha detectors are located behind the limiter shadow. Schematic diagram of the TFTR lost alpha detector. The escaping alphas enter a pair of apertures that disperse them in pitch angle and gyroradius (Darrow *et al.*, 1996a).

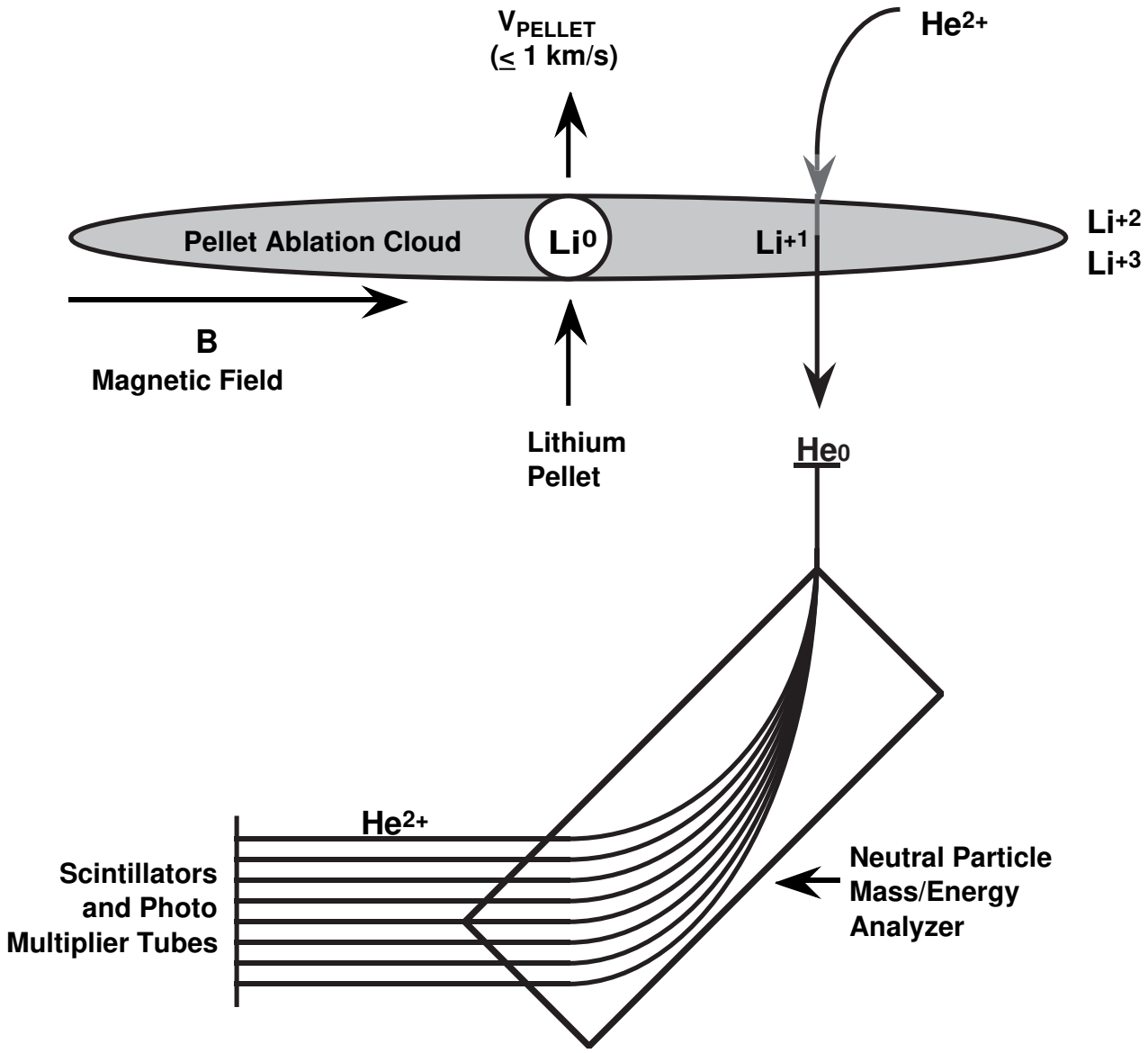

Fig. 6 Illustration of the pellet charge exchange diagnostic to measure confined alpha particles (Medley *et al.,* 1996b).

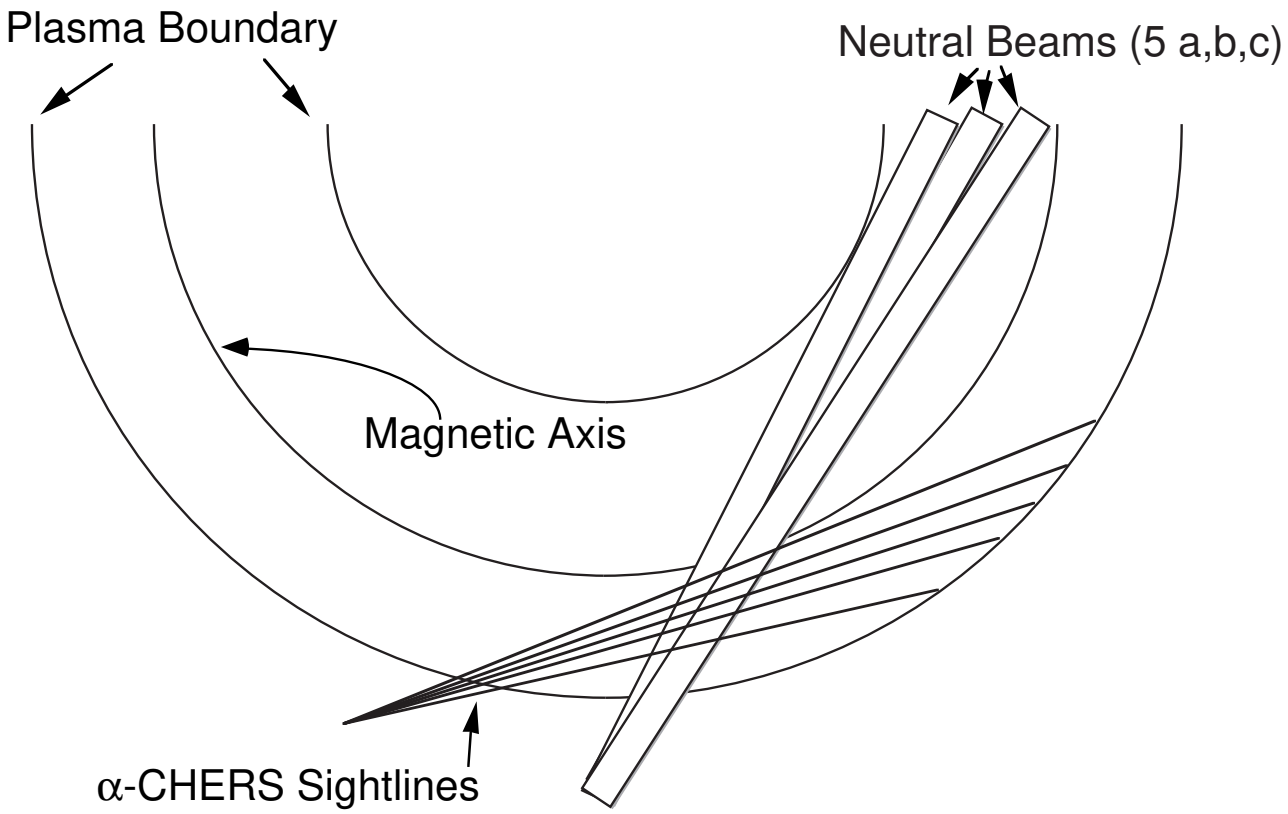

Fig. 7 Alpha-CHERS sightlines and beam viewing geometry (McKee *et al.,* 1995a, 1996).

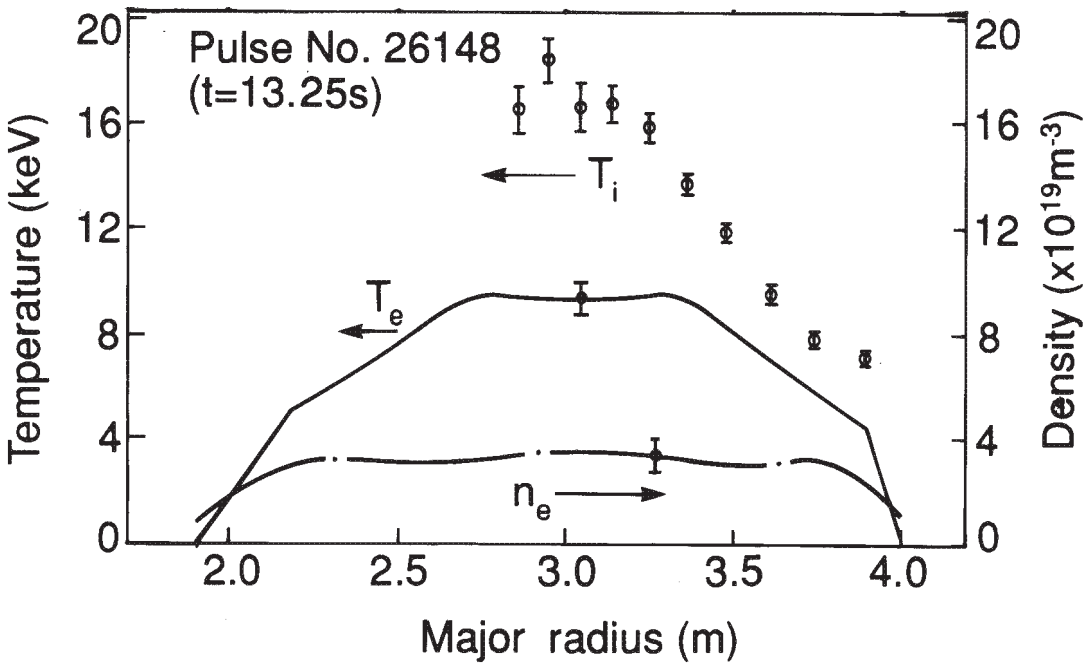

Fig. 8 Radial profiles of the ion and electron temperature and electron density for JET pulse number 26148 (JET Team, 1992).

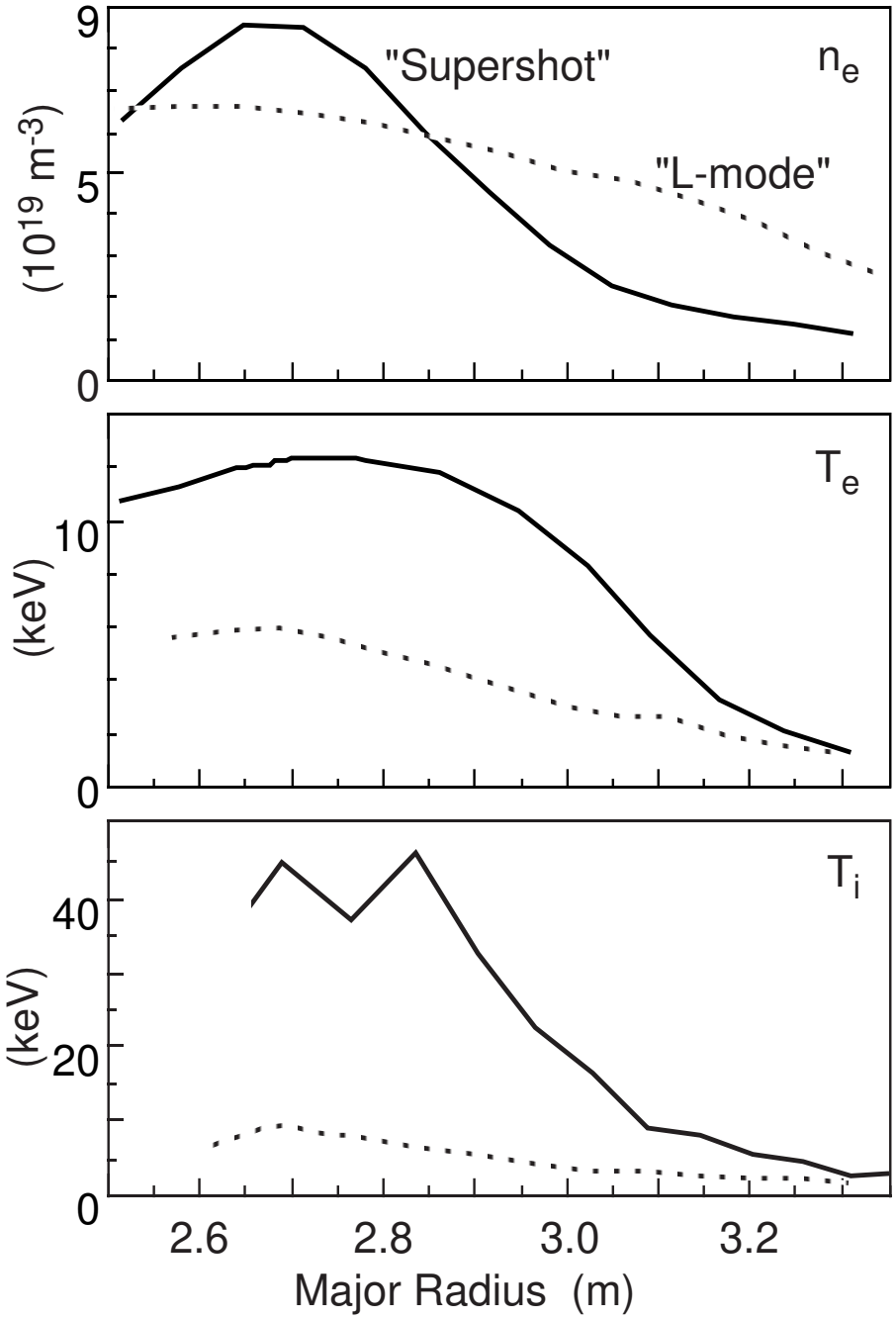

Fig. 9 Radial profiles of the ion and electron temperature and electron densities for TFTR pulse number 83546, a high performance supershot, is contrasted with a comparable L-mode discharge with similar plasma current and heating power.

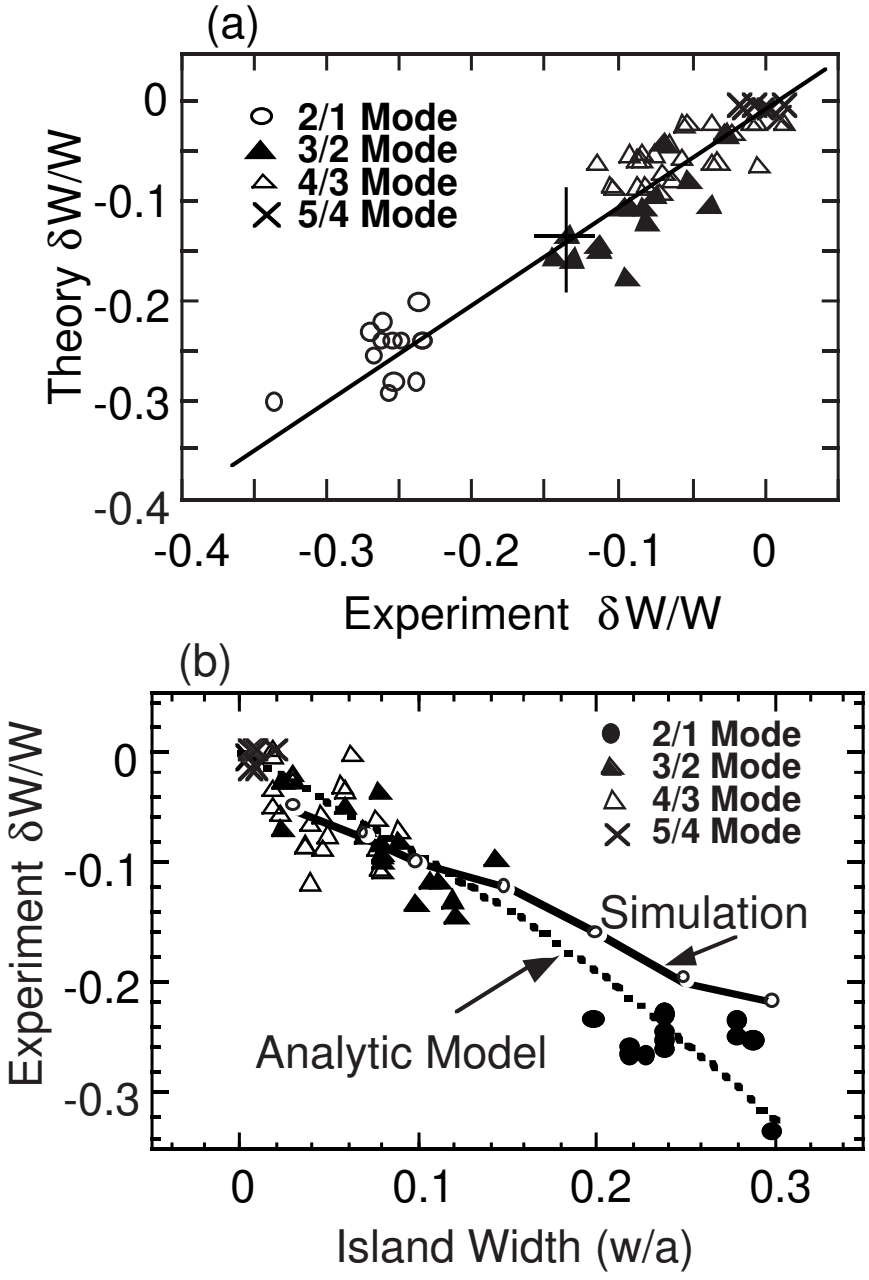

Fig. 10 (a) Comparison of stored energy deterioration (δW/W) theory and experiment due to neoclassical tearing modes. (b) The energy deterioration is proportional to the island width as predicted by the theory and simulation (Chang *et al.,* 1994).

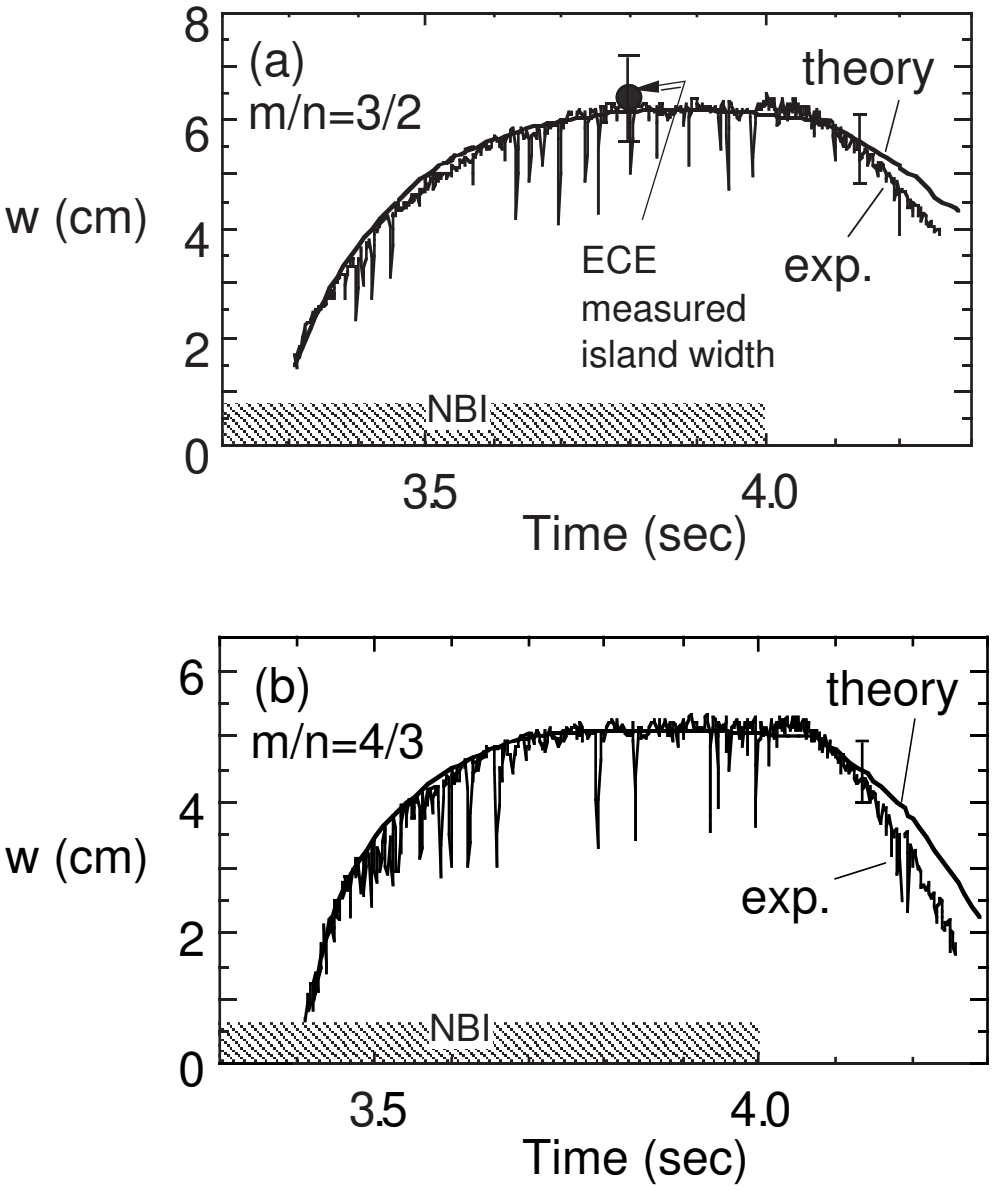

Fig. 11 Comparison of the measured magnetic island evolution with the nonlinear neoclassical p-driven tearing mode theory for (a) the m/n=3/2 mode case and (b) the 4/3 mode case (Chang *et al.,* 1994).

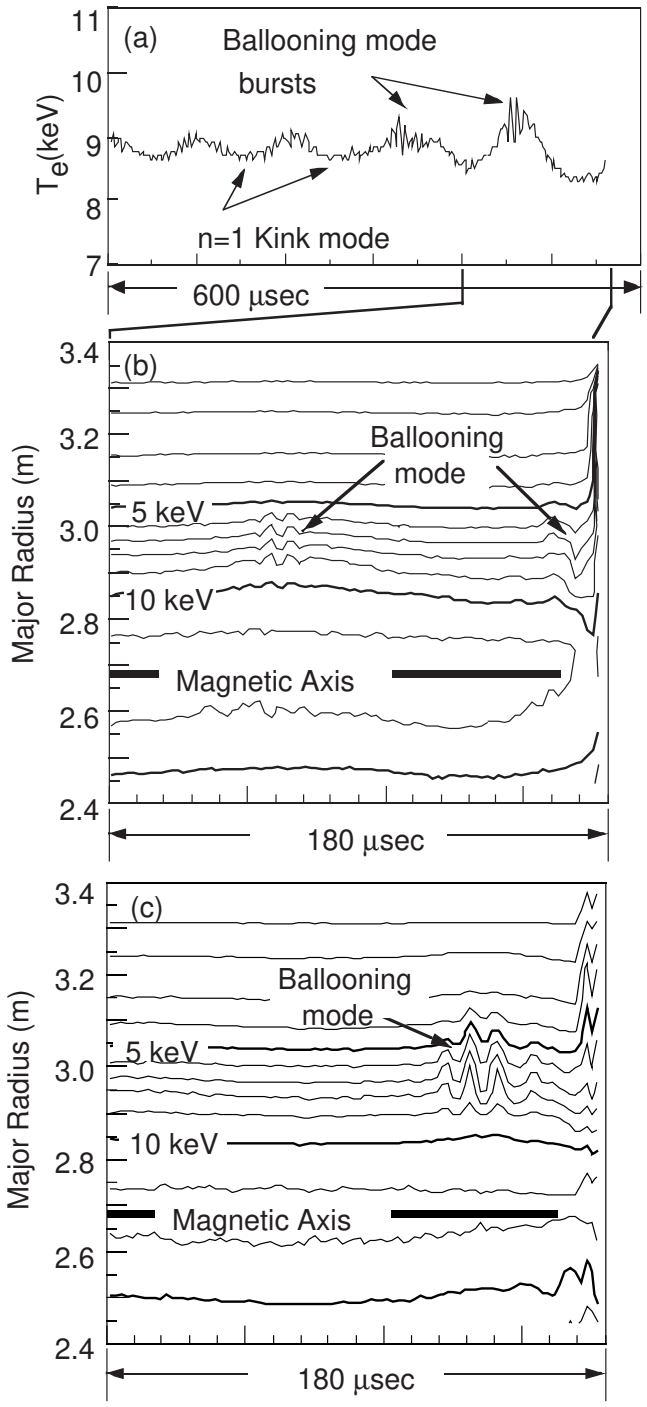

Fig. 12 a) Electron cyclotron emission measurements of the evolution of the electron temperature prior to a disruption. An n = 1 kink mode is observed to precede the destabilization of a ballooning mode (Fredrickson *et al.,* 1995a, 1996c).

b) Contours of the electron temperature evolution at one toroidal location. The ballooning mode is observed on the outer midplane.
c) Contours of the electron temperature evolution toroidally separated by 126^{o} from the previous set of measurements.

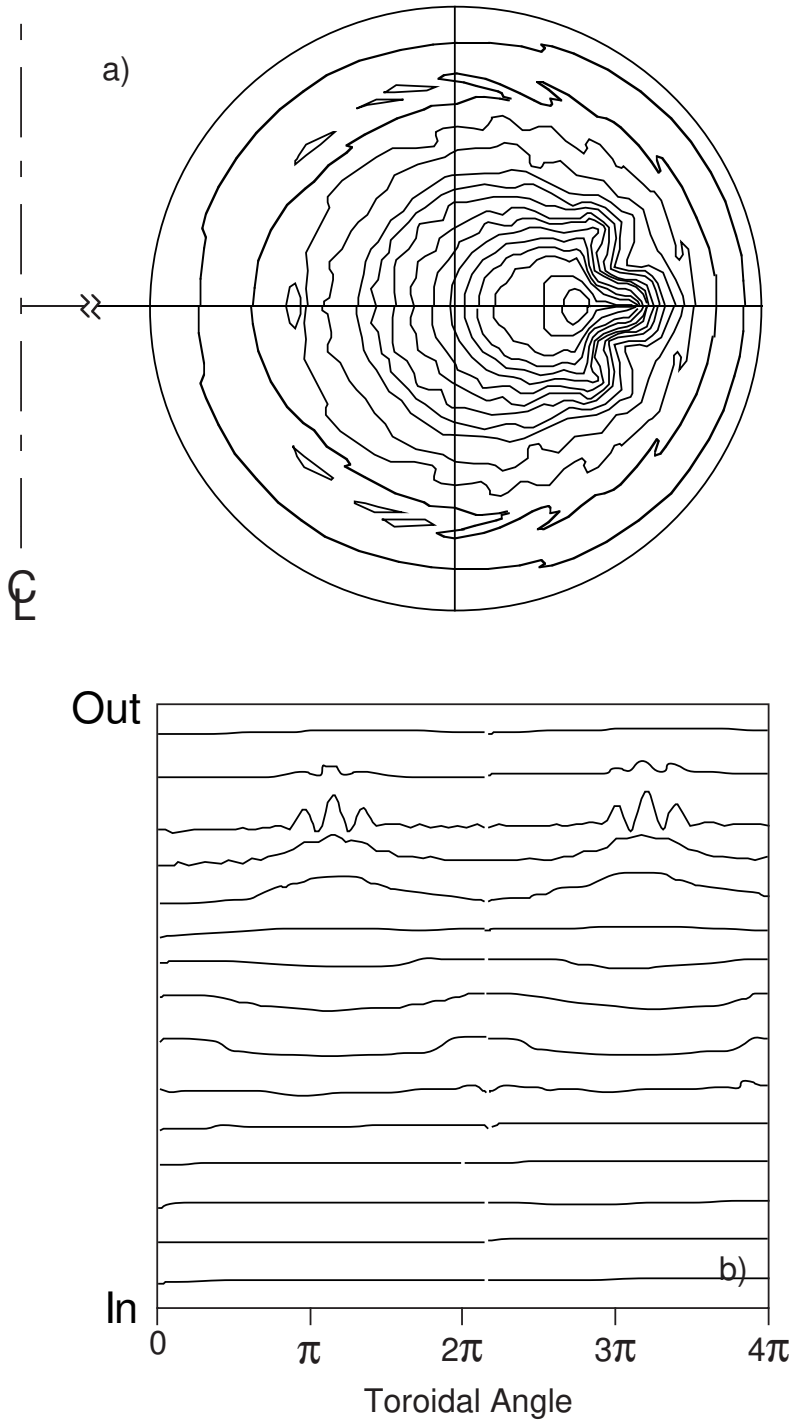

Fig. 13 a) Three dimensional nonlinear simulation of equi-pressure contours of the MHD instability.

b) Simulations of the electron cyclotron emission measurements of the electron temperature reproduce the observation of the ballooning mode shown in Fig. 12 being destabilized by a low-n kink mode with the largest displacement on the outboard side of the plasmas (Park *et al.,* 1995). Since the plasma rotates toroidally, the calculations versus toroidal angle are related to the measurements versus time.

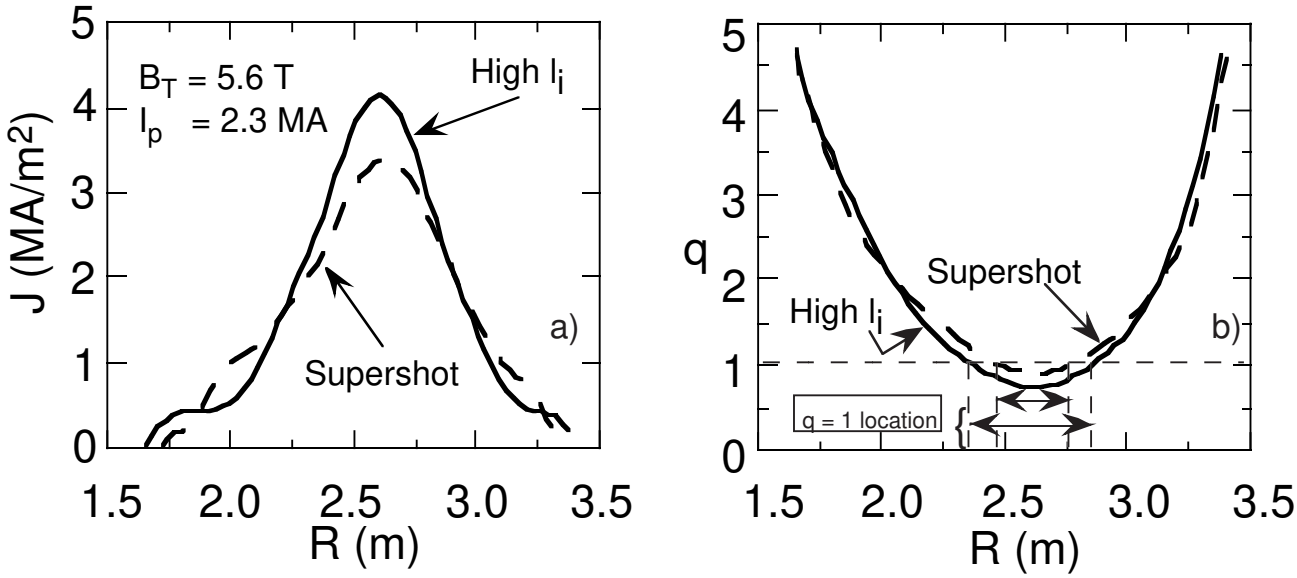

Fig. 14 Motional Stark Effect measurements of the j(r) and q(r) profiles in a high ℓ_i discharge are contrasted with a supershot discharge (Sabbagh *et al.,* 1996).

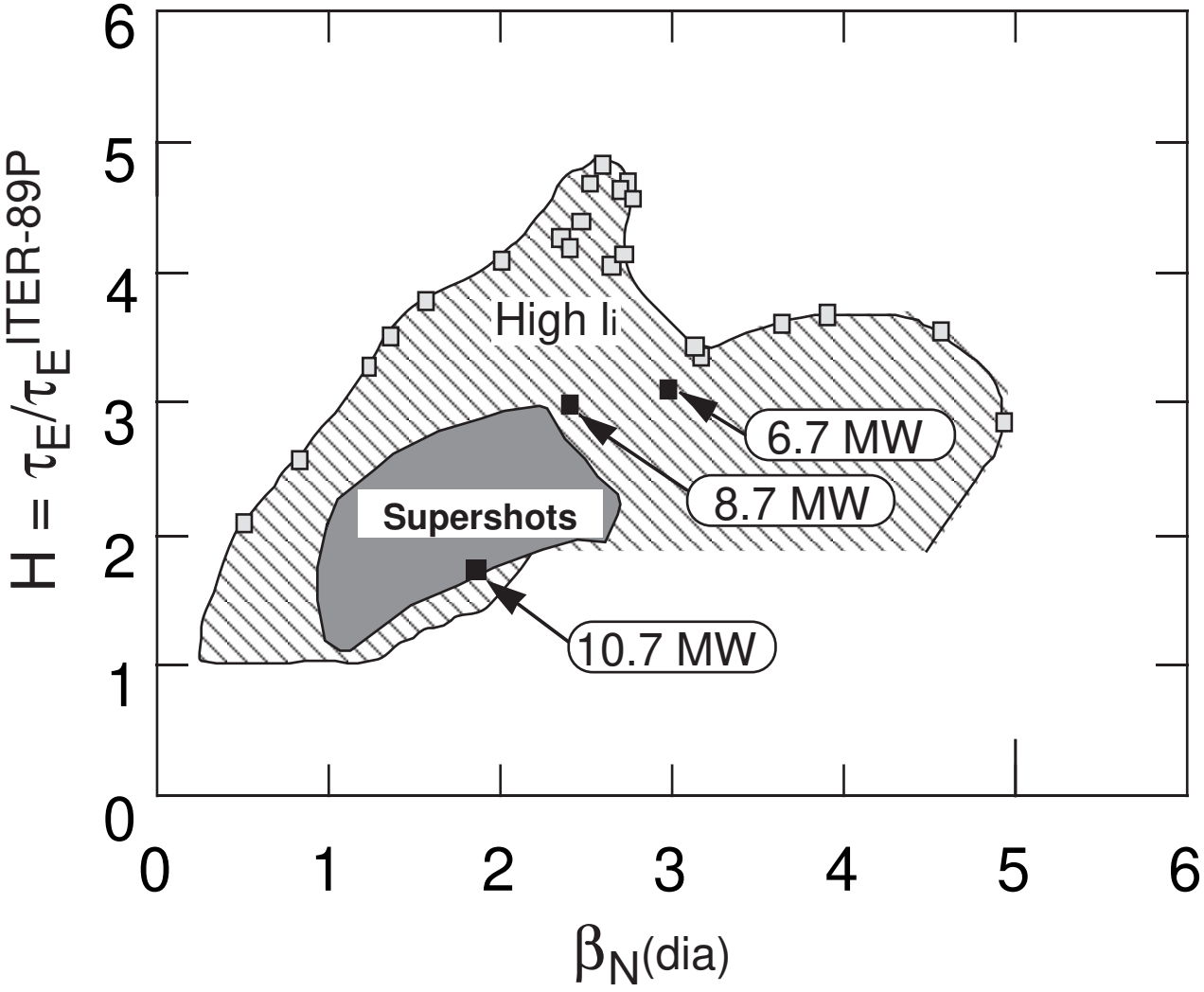

Fig. 15 Operating range of high ℓ_i discharges in terms of the enhancement in energy confinement time, $H = \tau_E/\tau_E^{ITER89\text{-}P}$ and β_N is compared with the operating range of supershot discharges (Sabbagh *et al.,* 1994b, 1996).

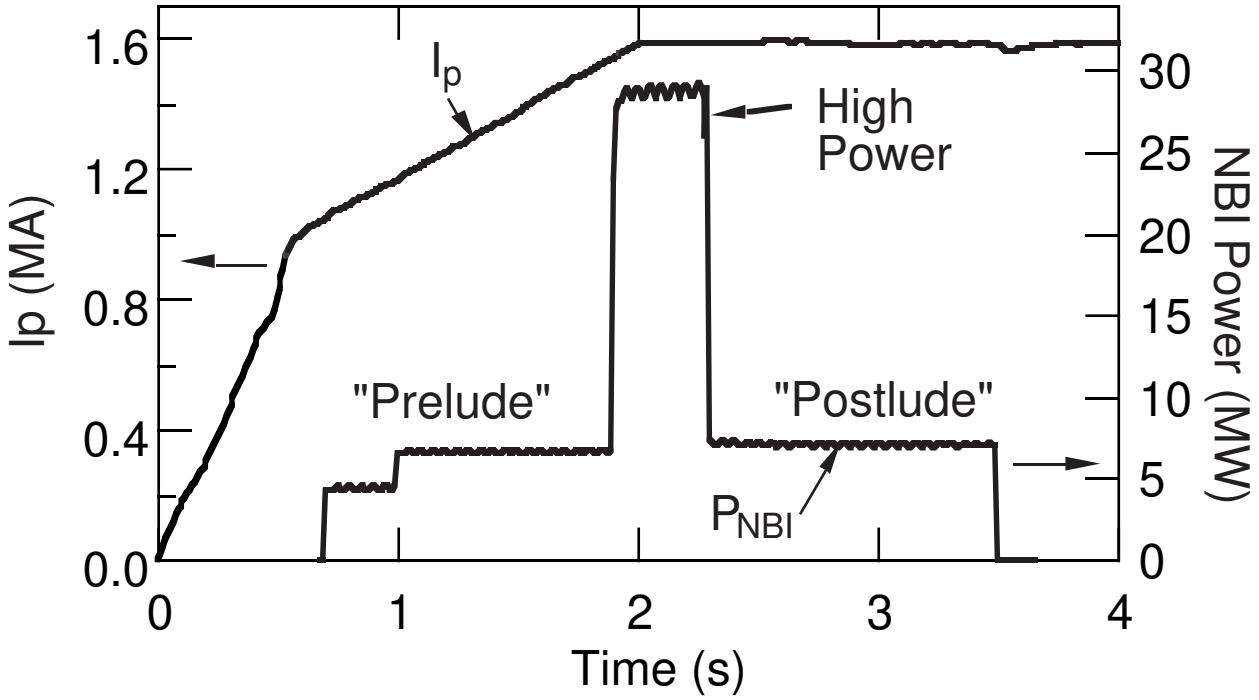

Fig. 16 Hollow current profiles are achieved by rapidly ramping the plasma current and heating the plasma in the "prelude" phase prior to the "high power" heating phase. Subsequently, the power is decreased in the "postlude" phase to study the evolution of the plasma transport (Levinton *et al.,* 1996).

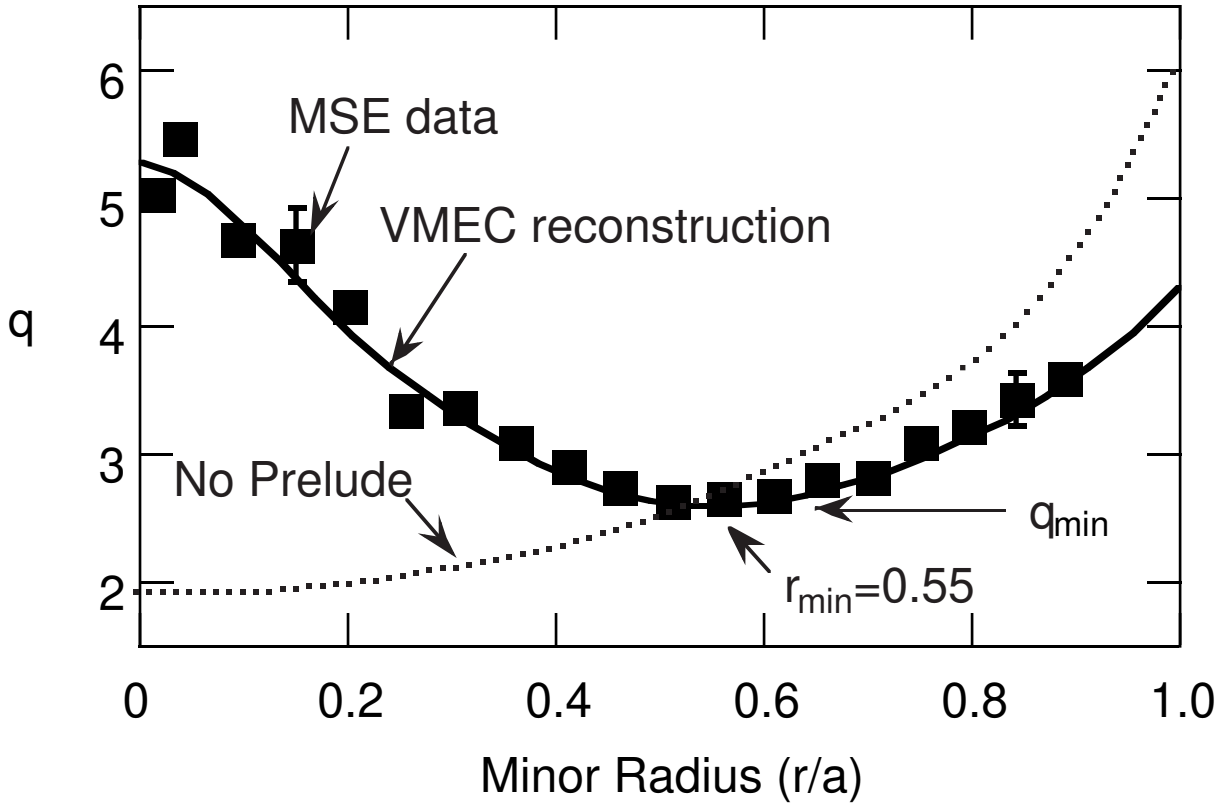

Fig. 17 Motional Stark Effect measurements of the safety factor, q, which illustrate the effect of applying heating power during the "prelude" phase. The magnetic equilibrium reconstruction analysis is shown for comparison. The normalized minor radius of the minimum of the safety factor is denoted r_{min} and the corresponding value of the safety factor is denoted q_{min} (Levinton *et al.,* 1996).

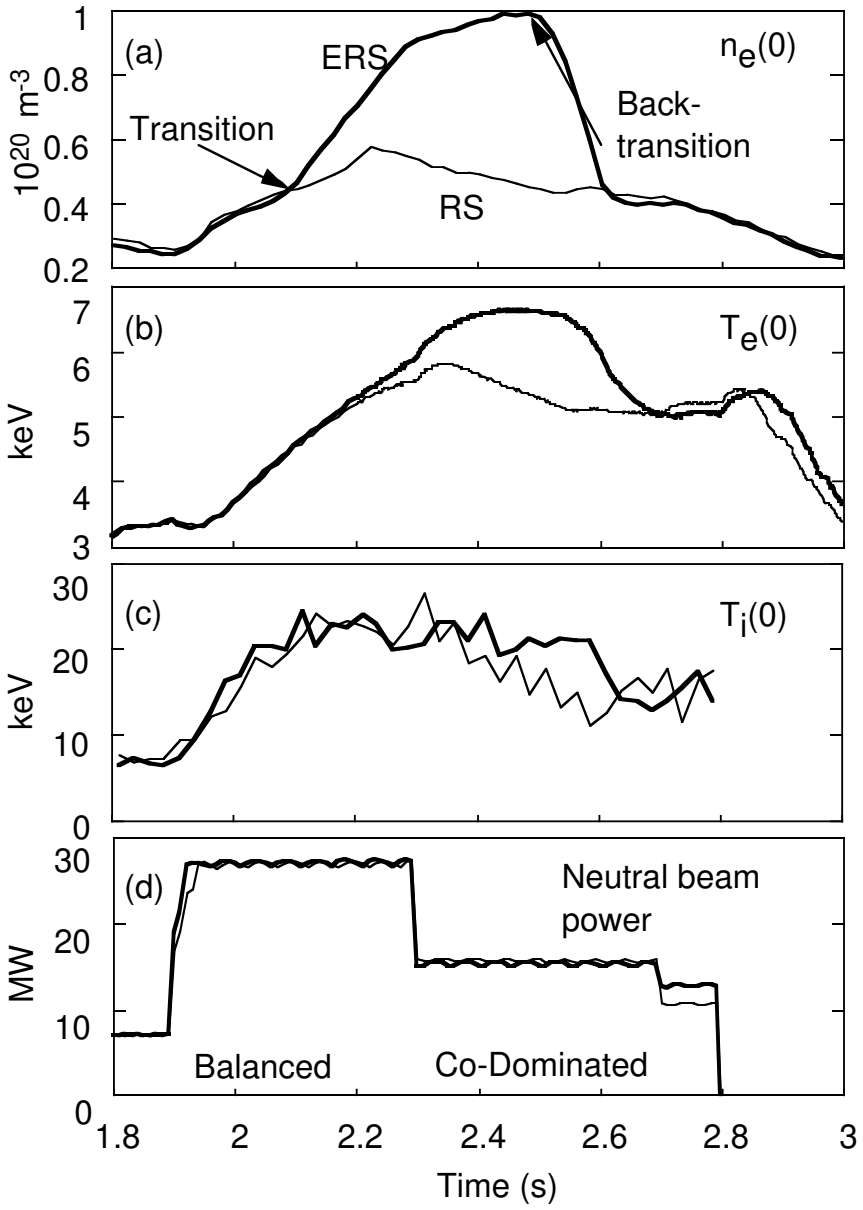

Fig. 18 Comparison of the evolution of two reverse shear discharges near the threshold power for a transition. Shown is the (a) central electron density, (b) the central electron temperature, (c) the central ion temperature, and (d) the total neutral beam power waveform. In the enhanced reverse shear discharge, the development of an internal transport barrier and reduced core transport results in a large increase in the central density and core pressure. In this ERS plasma, the loss of good core confinement in the 14 MW "postlude" period of injection is correlated with a reduction in the radial electric field magnitude **ExB** shearing rate γ_s, induced by opposing contributions from co-rotation and the plasma pressure (Synakowski *et al.,* 1996a) After the back transition, the plasma confinement properties return to those in the reverse-shear discharge without the transport barrier.

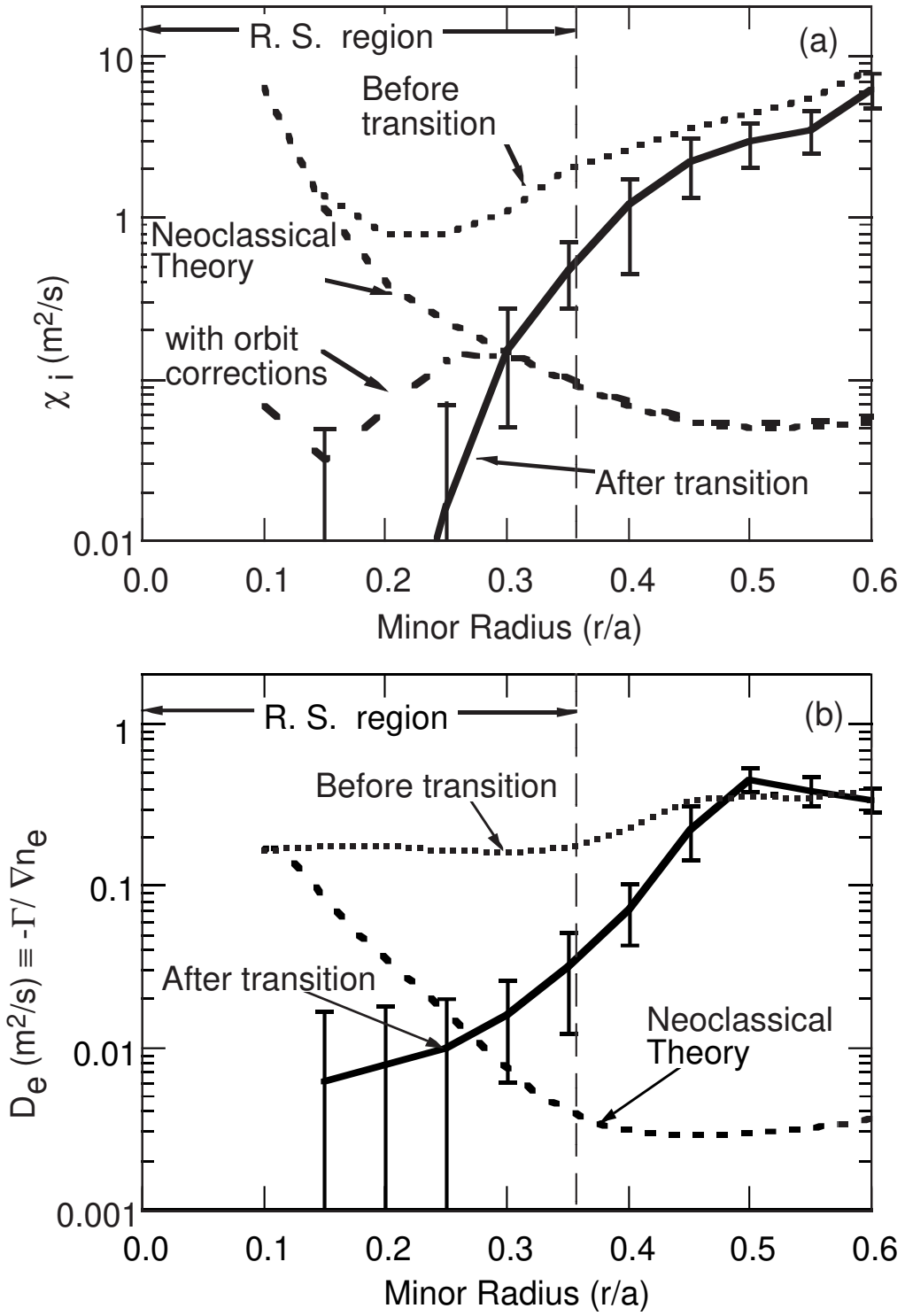

Fig. 19 The inferred ion thermal diffusivity (a) and particle diffusivity (b) is observed to decrease dramatically in the enhanced reversed shear discharges (Levinton *et al.*, 1995). For comparison, the standard calculation of neoclassical ion heat conductivity is shown as well as the recent calculations by Lin *et al.* (1996).

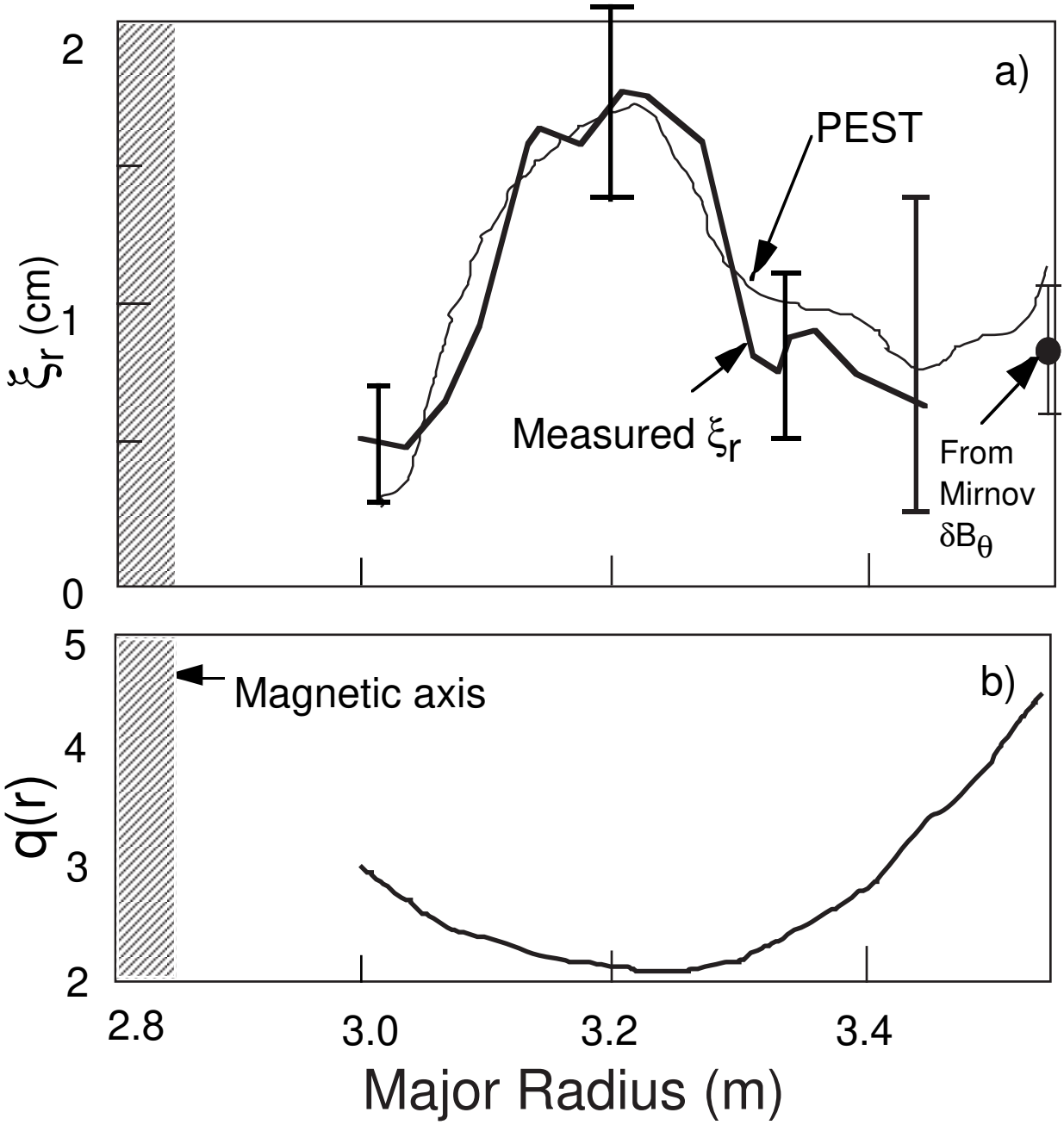

Fig. 20 a) ECE measurements of the displacement of the magnetic surfaces are in good agreement with the predictions of ideal MHD theory for reverse shear TFTR discharges (Manickam *et al.,* 1996). b) The corresponding q-profile.

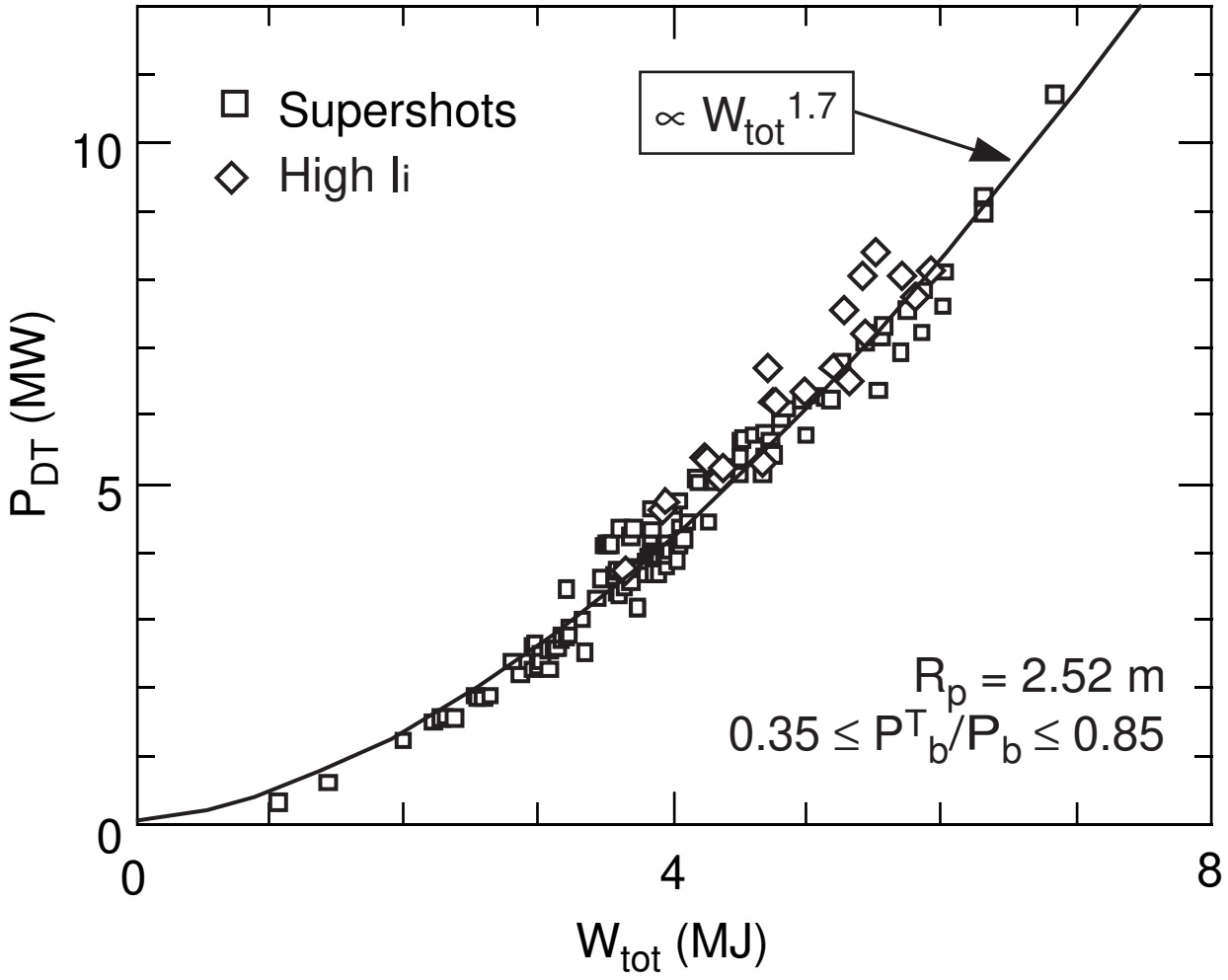

Fig. 21 Dependence of the peak D-T fusion power (averaged over a 40ms interval) on total plasma energy in high-current (≥ 2.0 MA) supershots [squares] and high-ℓ_i plasmas at 2.0 - 2.3 MA produced by cross-section expansion of low-q ($q_a \approx 2.5$) discharges [diamonds]. All plasmas have approximately the same volume (~ $38m^3$) and a nearly optimal mixture of D and T in the reactive region produced by neutral beam injection (Bell *et al.*, 1996).

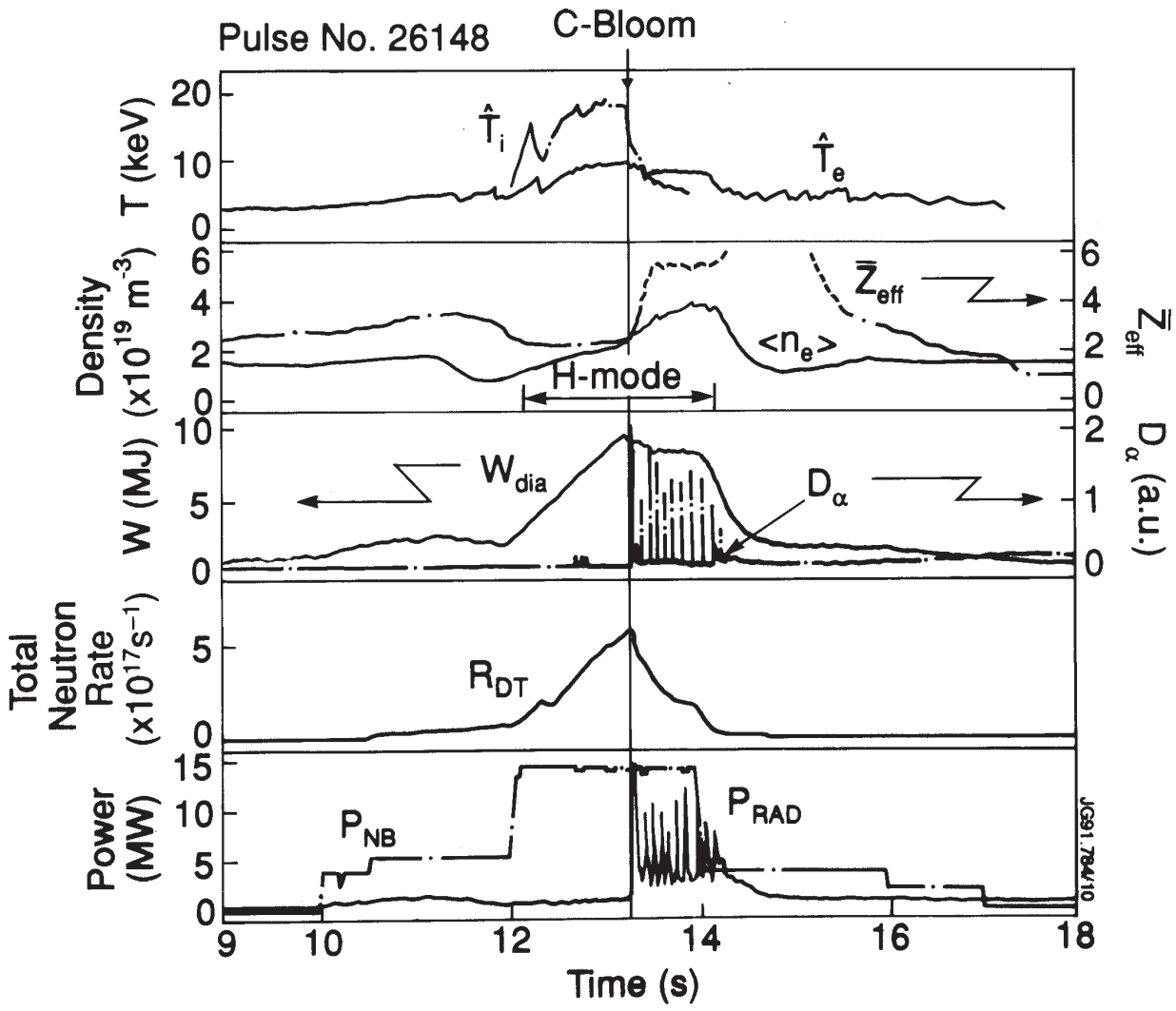

Fig. 22 Time dependence of the central electron and ion temperatures, the volume averaged electron density, the line average, Z_{eff}, the plasma diamagnetic energy, the $D\alpha$ emission, the total neutron rate, and the neutral beam and radiated power for pulse No. 26148 (JET Team, 1992).

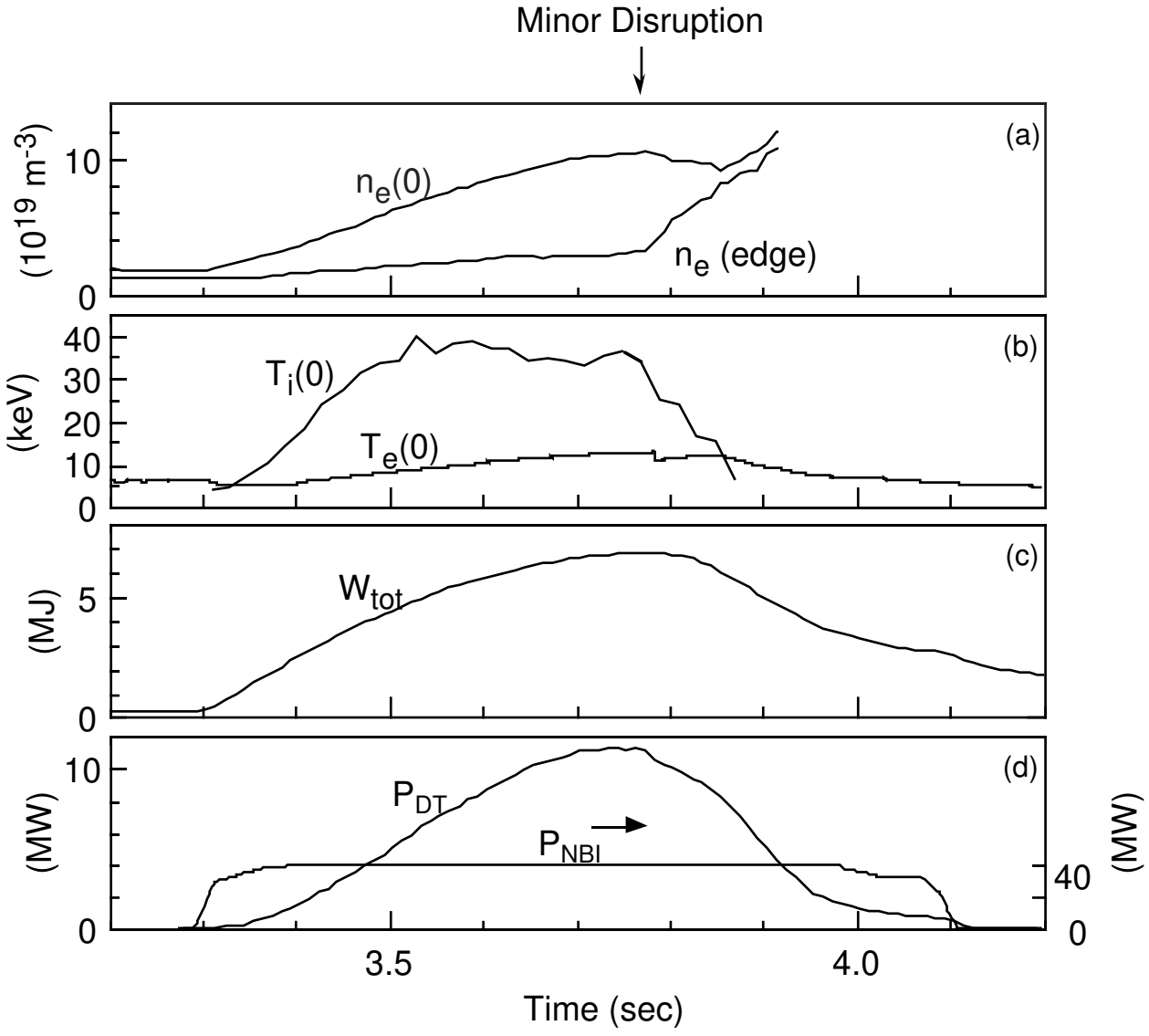

Fig. 23 Evolution of the central electron density, ion temperature, electron temperature, stored energy and fusion power for TFTR shot No. 80539.

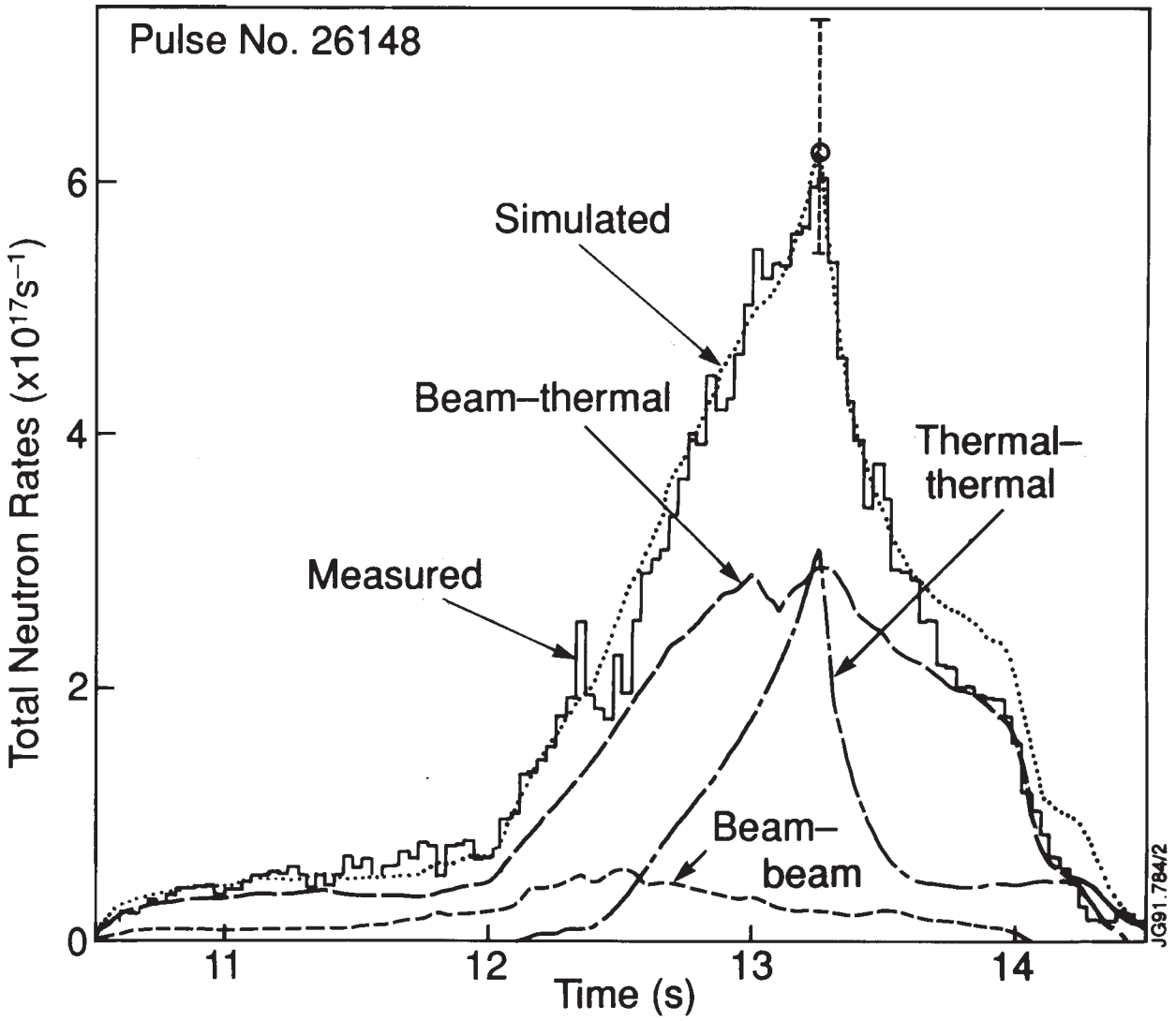

Fig. 24 Neutron source strength measurements and TRANSP simulation of the total neutron rate on JET pulse No. 26148 (JET Team., 1992).

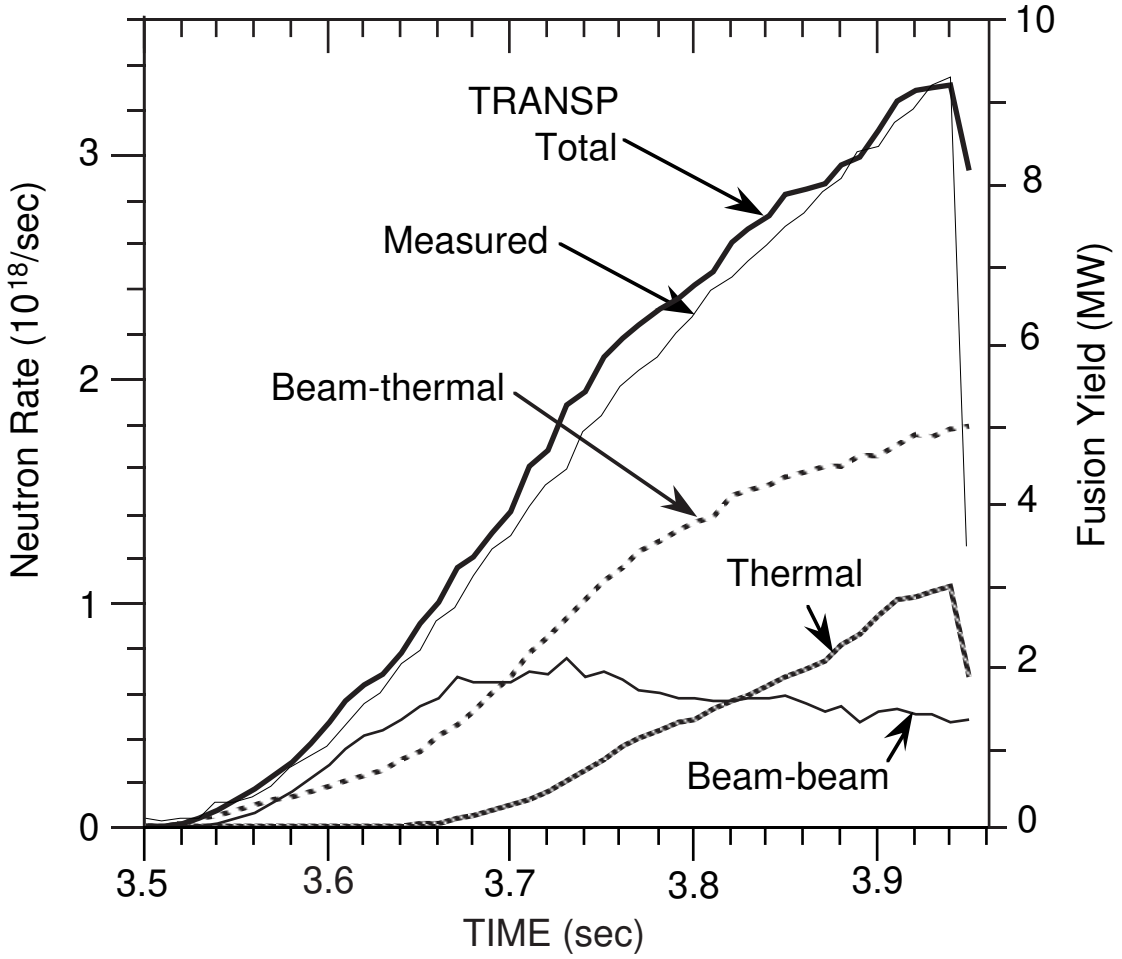

Fig. 25 Neutron source strength measurement and TRANSP simulation of the total neutron rate for TFTR pulse No. 76778 with P_b = 33.9 MW (Budny *et al.,* 1995).

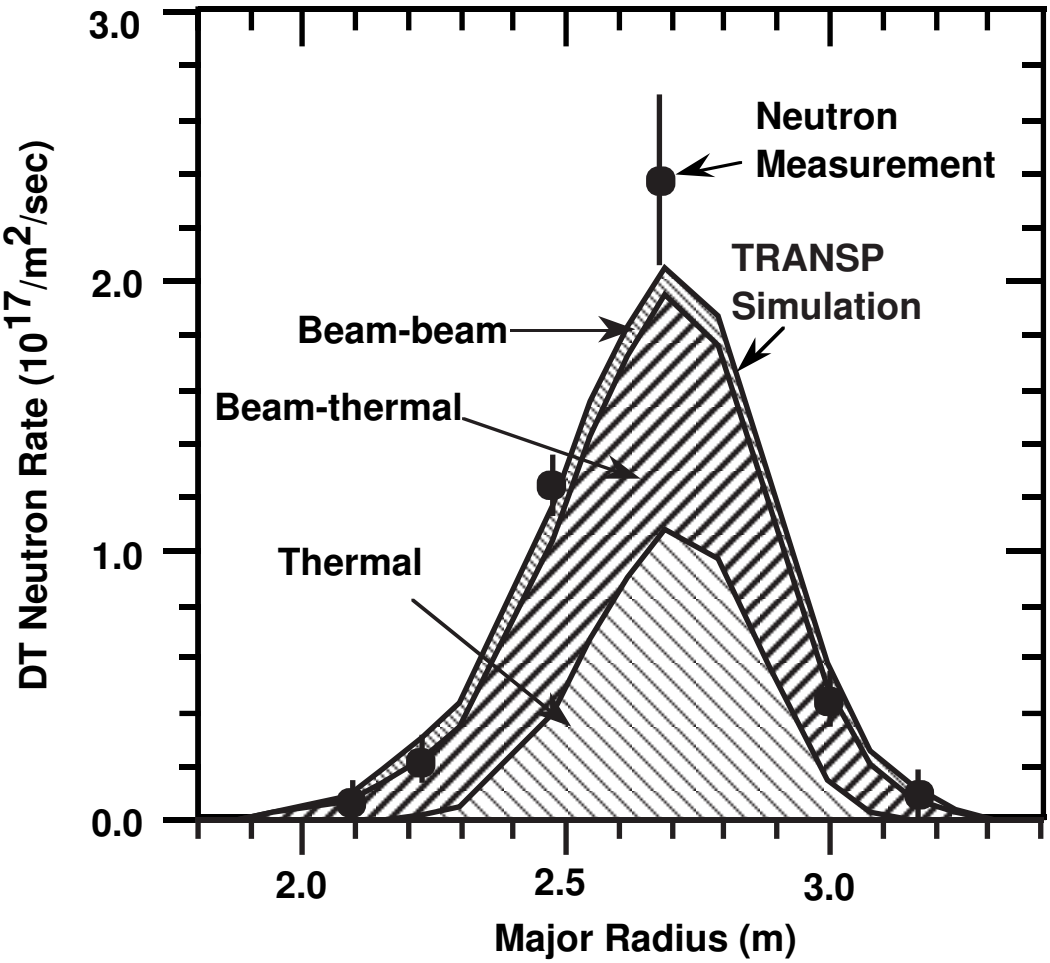

Fig. 26 Neutron emission profile as measured by the neutron collimator are compared with a TRANSP simulation. The contributions from thermal-thermal, beam-thermal and beam-beam reactions are shown (Budny *et al.,* 1995).

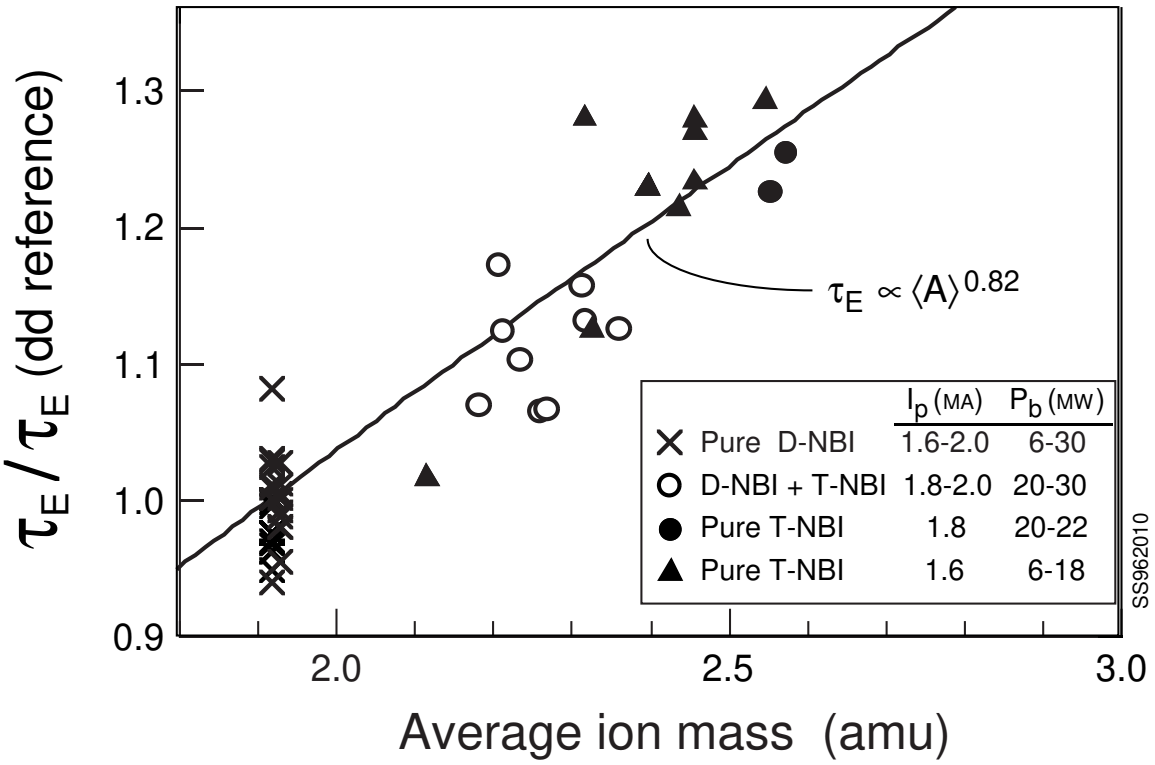

Fig. 27 The ratio of the energy confinement in a D-T discharge is compared with that in a companion D-discharge versus the average hydrogenic ion mass, $\langle A \rangle = \Sigma n_i A_i / \Sigma n_i$, where n_i is the hydrogenic density (Scott *et al.,* 1995, 1996a).

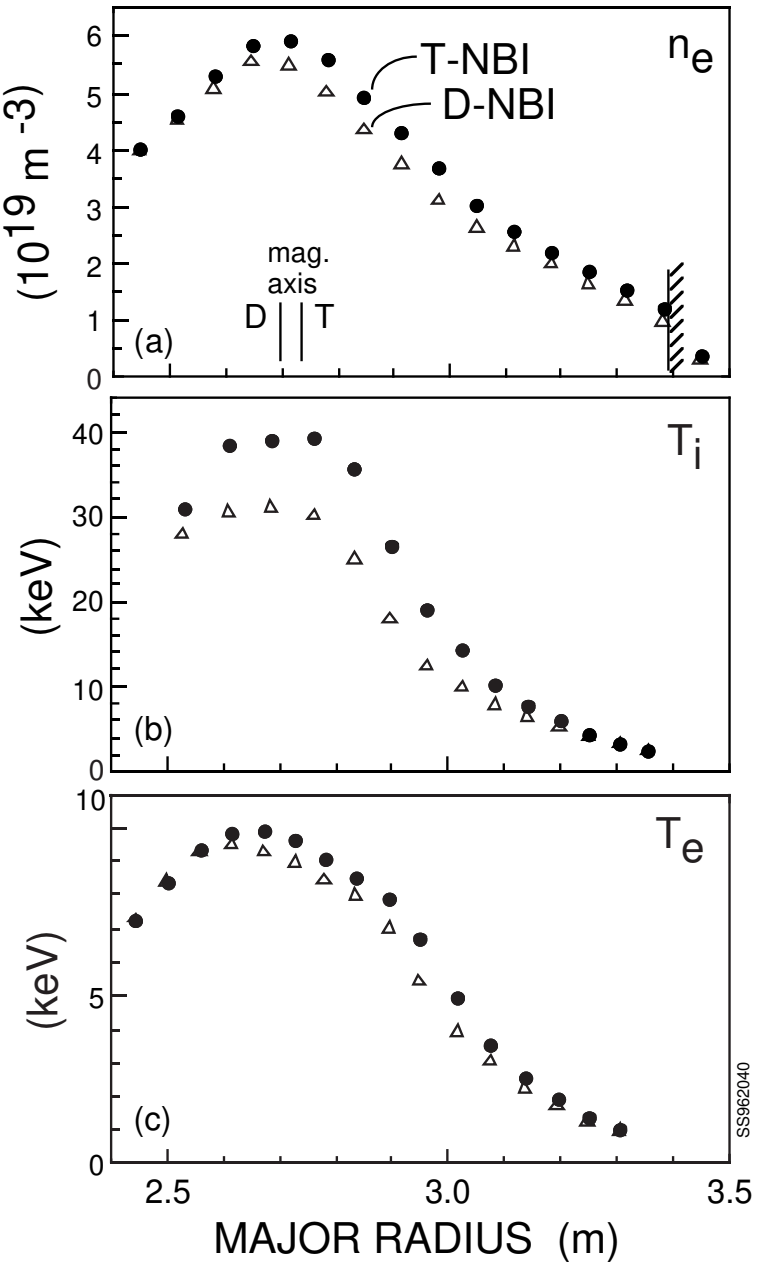

Fig. 28 Comparison of electron density, ion and electron temperature profiles for a D and a companion D-T discharge (Scott *et al.,* 1996a).

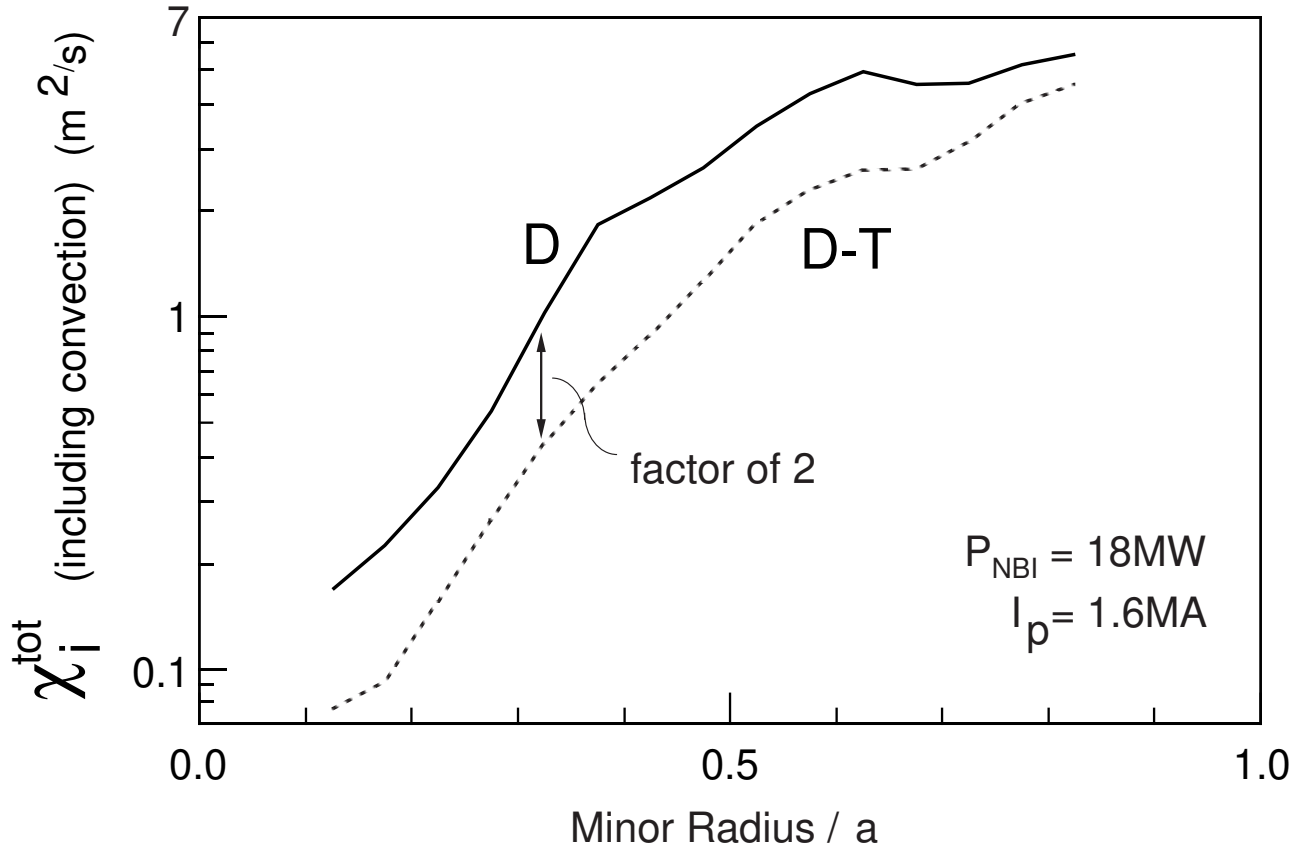

Fig. 29 Comparison of the ion thermal diffusivity in a D-T plasma heated by tritium beam with a companion D discharge. The thermal mix of the background ions is approximately a 50:50 D-T mix. (Scott *et al.,* 1996a).

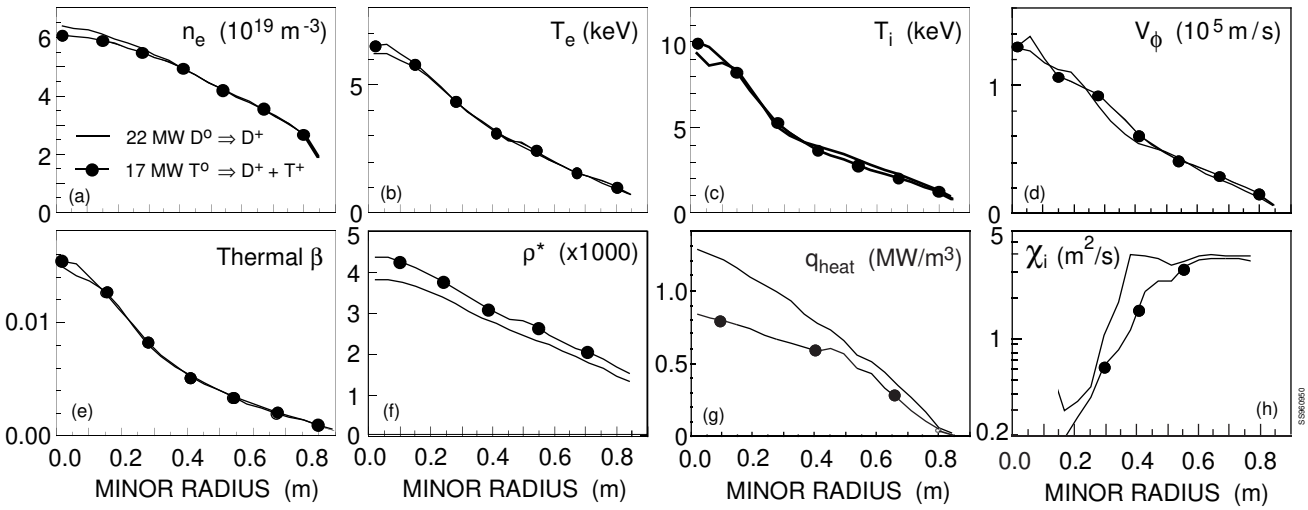

Fig. 30 Kinetic profiles in D and D-T L-mode 'isotope ρ*-scaling' plasmas matched in density, temperature, β, ν*, B_t, I_p, Z_{eff}, and $\nu*_e$. Contrary to gyroBohm expectations, the D plasma with smaller ρ_* requires ~ 30% more heating power to sustain the temperature (Scott *et al.,* 1996b).

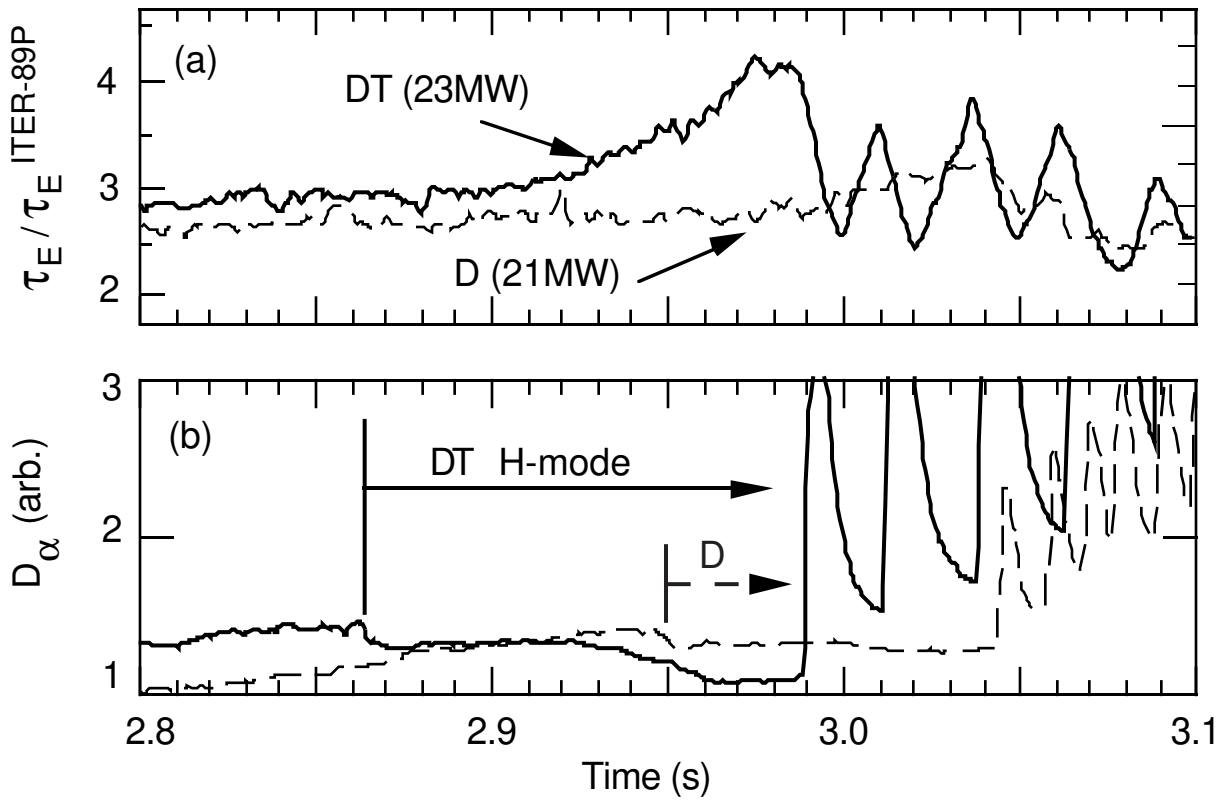

Fig. 31 Evolution of a) $\tau_E/\tau_E^{ITER-89-P}$ and b) D_α for a D-T discharge and a companion D discharge on TFTR (Bush *et al.,* 1995).

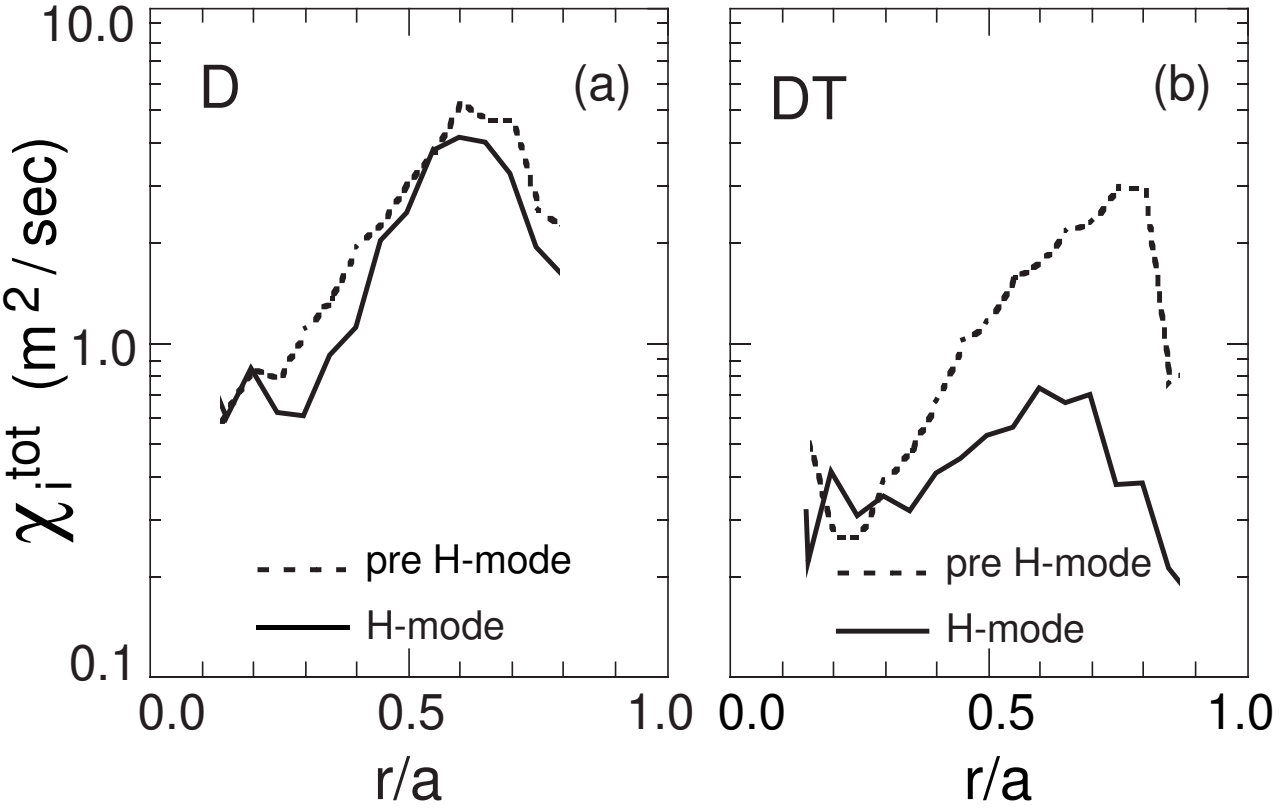

Fig. 32 Comparison of the effect of H-mode transition in a D and D-T limiter discharge on TFTR (Bush *et al.,* 1995).

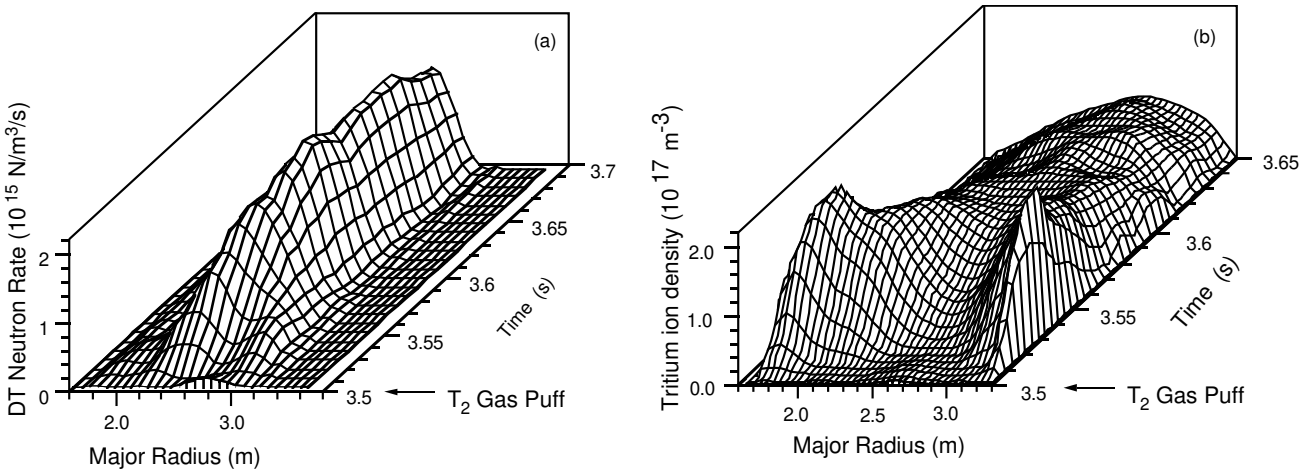

Fig. 33 Evolution of a) D-T neutron emissivity and b) the inferred tritium density profiles following a small tritium gas puff into a supershot discharge on TFTR (Johnson *et al.,* 1994; Efthimion *et al.,* 1995a).

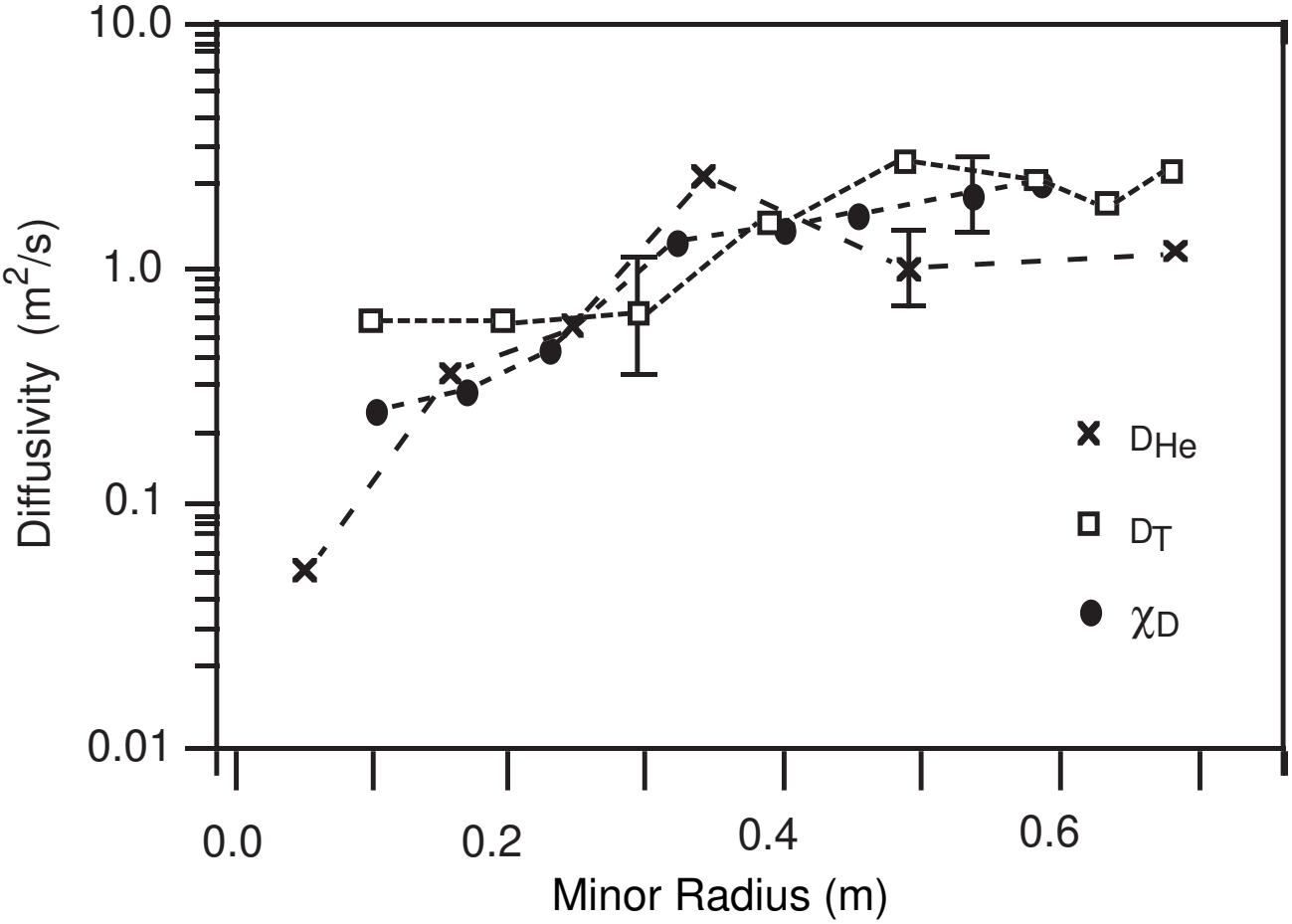

Fig. 34 The tritium particle diffusivity following a small tritium gas puff is comparable with the electron particle diffusivity as well as the He diffusivity (Efthimion *et al.,* 1995a).

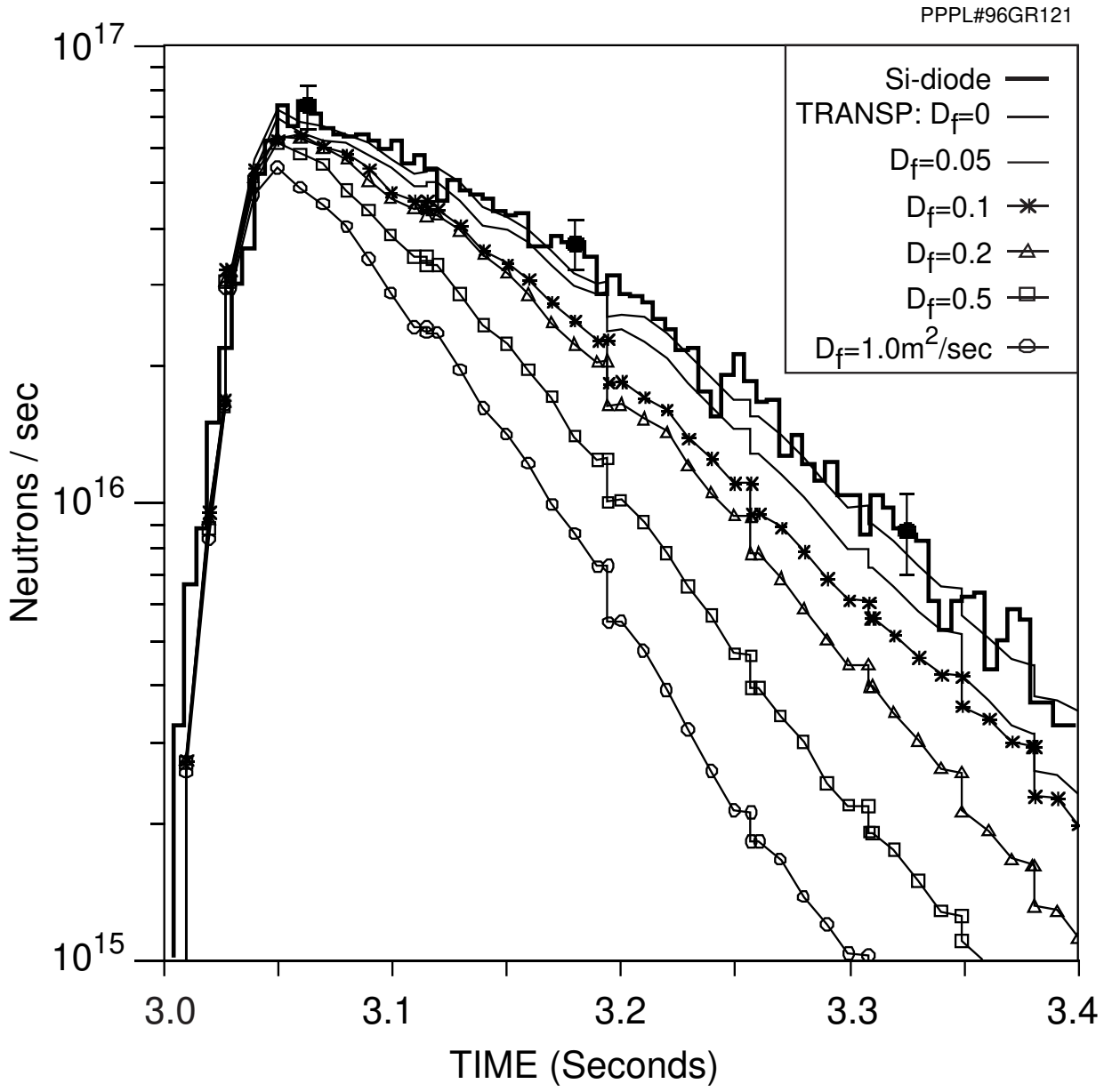

Fig. 35 The measured neutron source strength of 14 MeV neutrons by a Si diode detector due to a short pulse of high power neutral beam injection is in good agreement with simulations which assume a small radial diffusivity ($D_f < 0.05 m^2/s$) for the beam ions (Ruskov *et al.,* 1995).

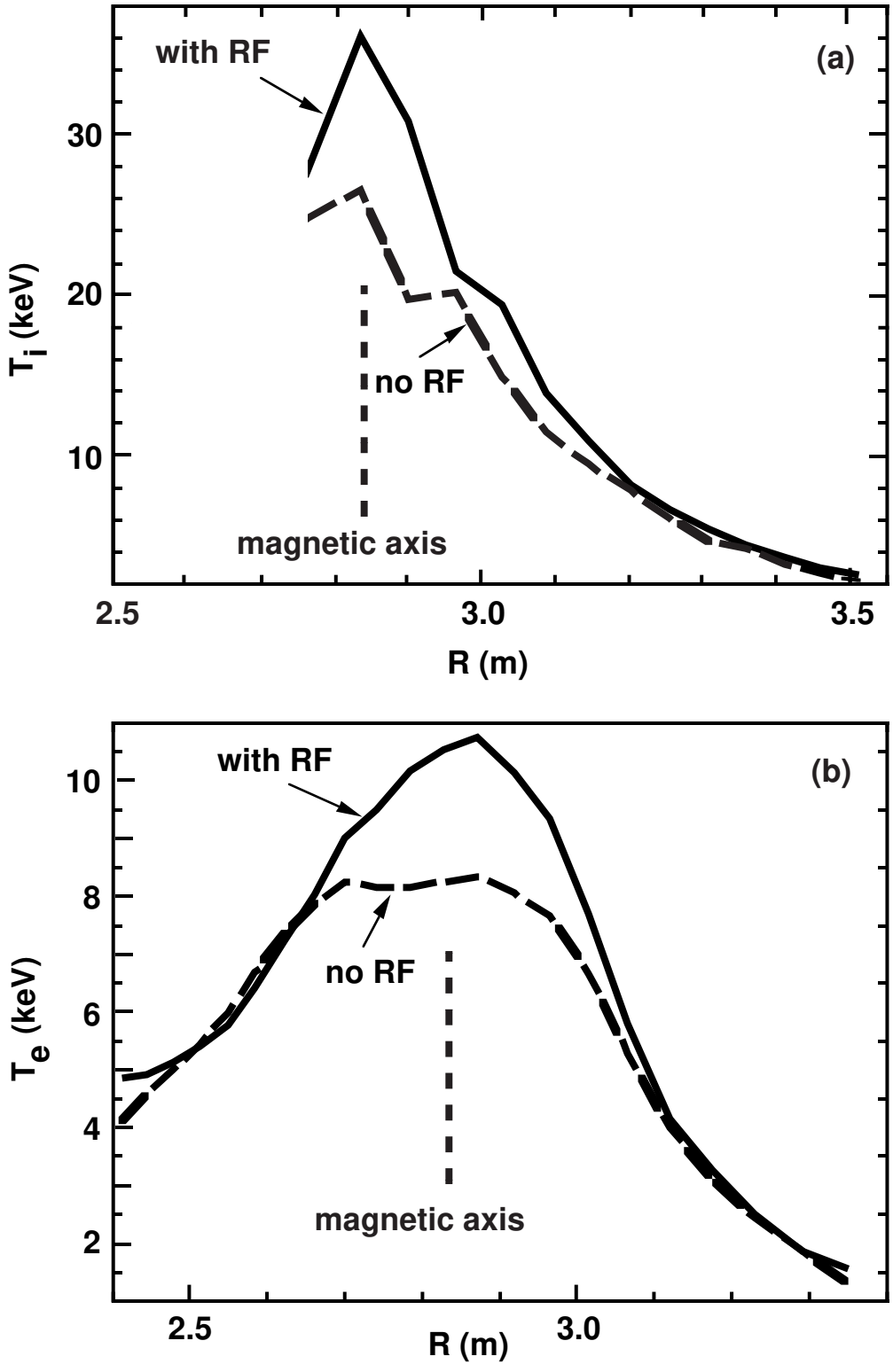

Fig. 36 Ion and electron temperature profiles in a discharge heated with 23.5 MW of neutral beam heating and in another supplemented by an additional 5.5 MW of ICRF heating (Wilson *et al.,* 1995).

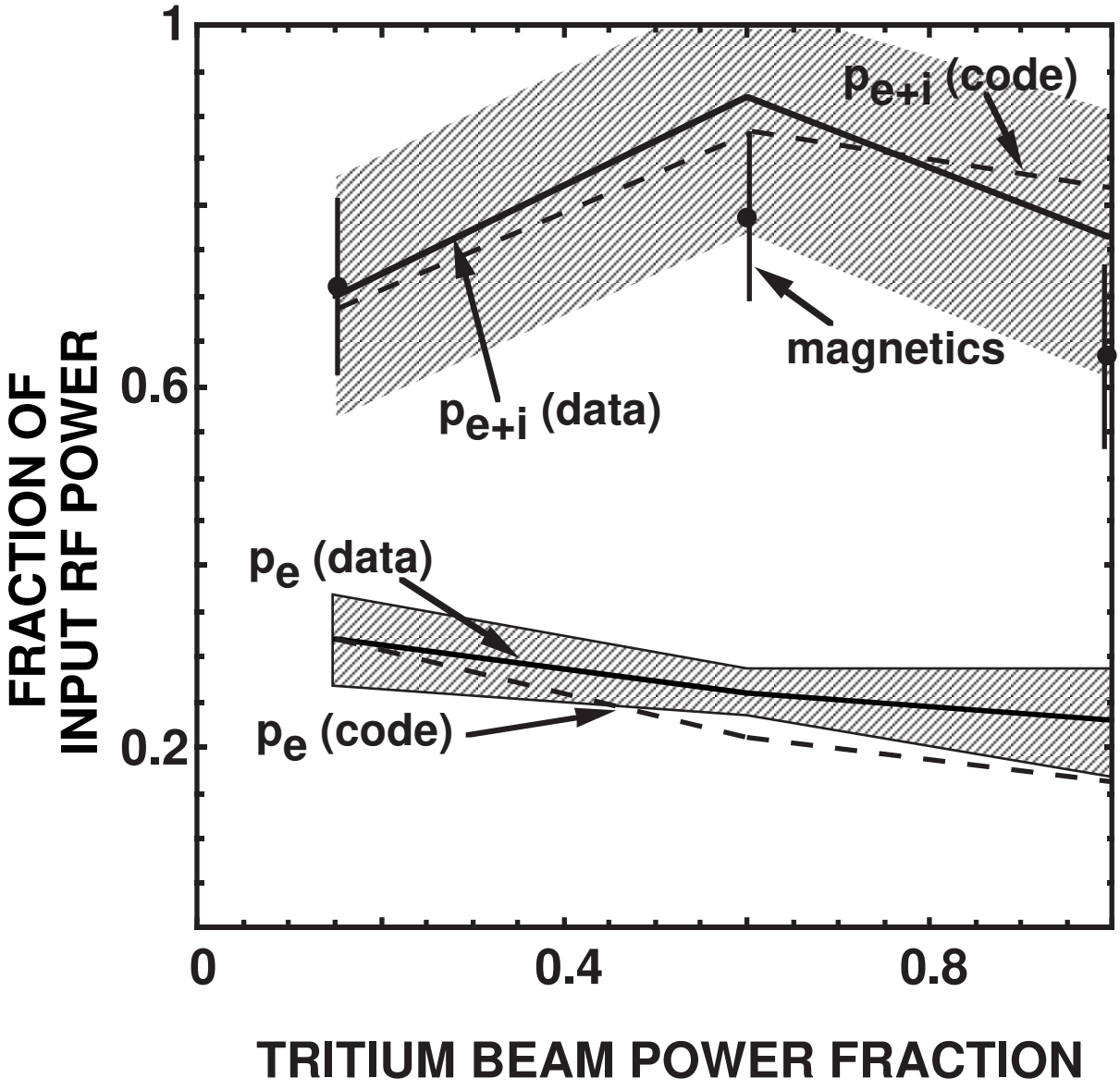

Fig. 37 Measurements and prediction using the PICES and TRANSP codes of the fraction of rf power absorbed by electron and ions versus the triton beam power fraction. Modulation of the rf power together with the evolution of the electron and ion temperature is used to infer the fraction of power absorbed by ions and electrons (Phillips *et al.,* 1995).

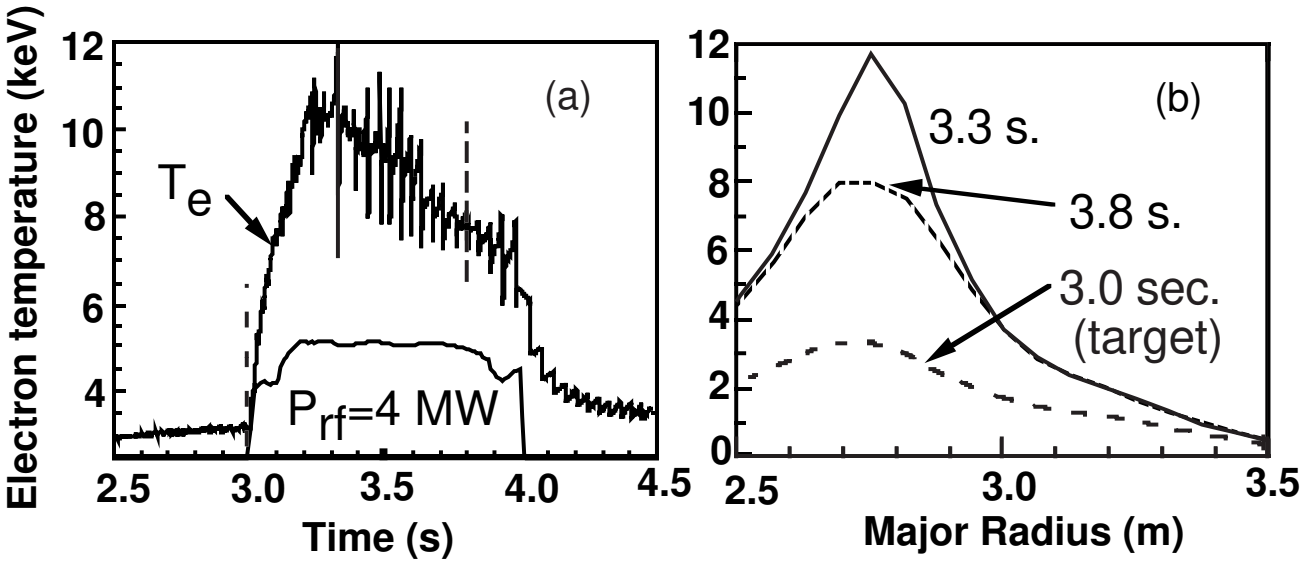

Fig. 38 Mode conversion of the fast wave results in strong and highly localized electron heating at the ion-ion hybrid layer (Majeski *et al.,* 1996).

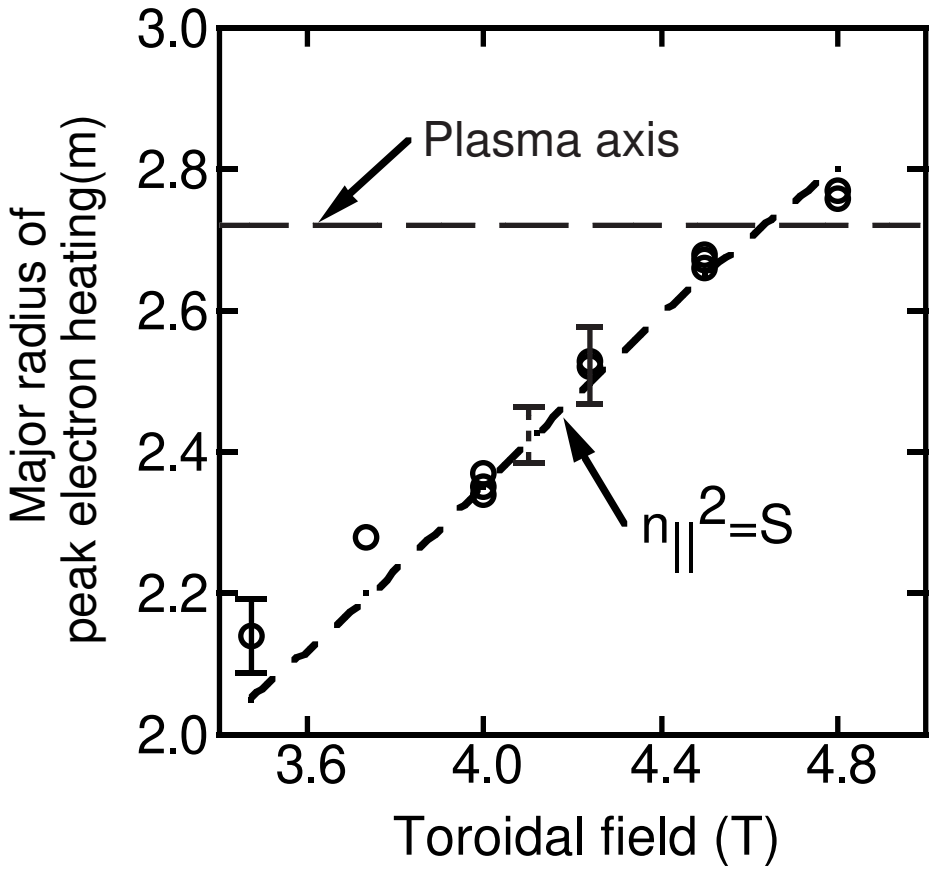

Fig. 39 Observed radius of electron power deposition as a function of toroidal field, for constant ^{3}He fraction and density. The open symbols denote the observed location from electron temperature measurement and the line denotes the location of mode conversion layer (Majeski *et al.,* 1996).

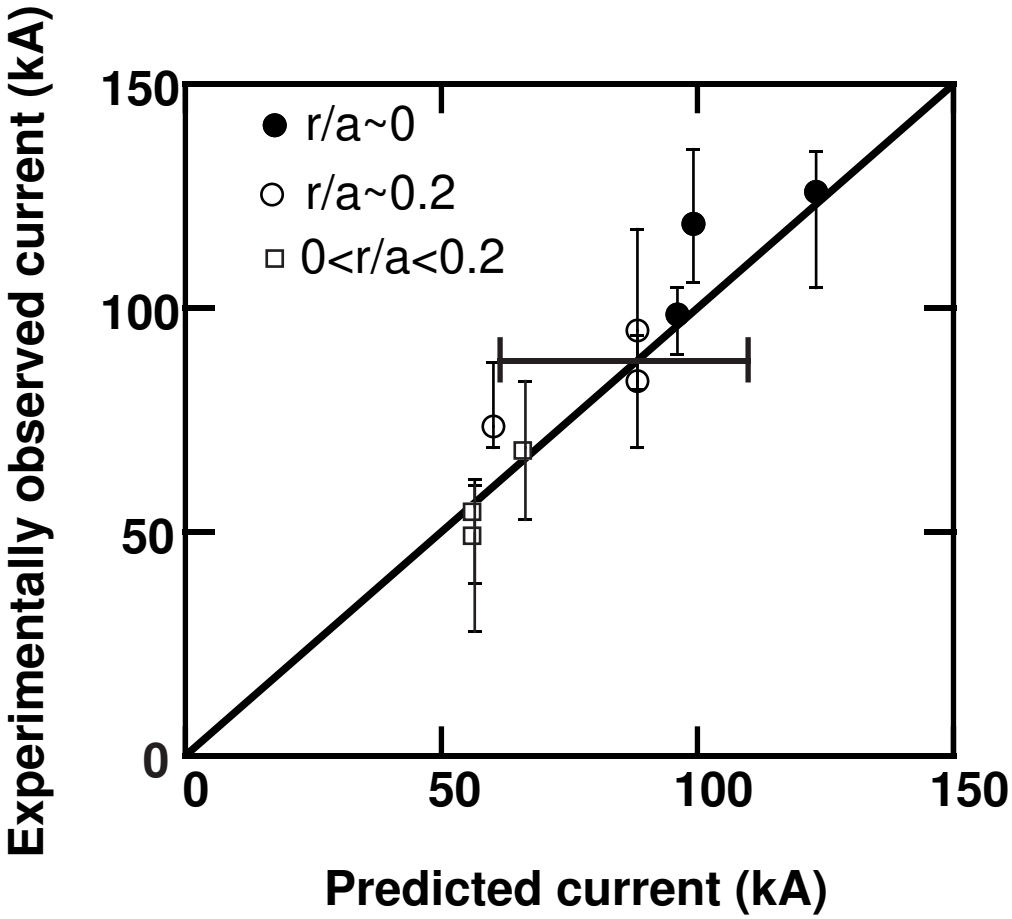

Fig. 40 The measured mode conversion current drive is compared with the predicted current drive (Majeski *et al.,* 1996).

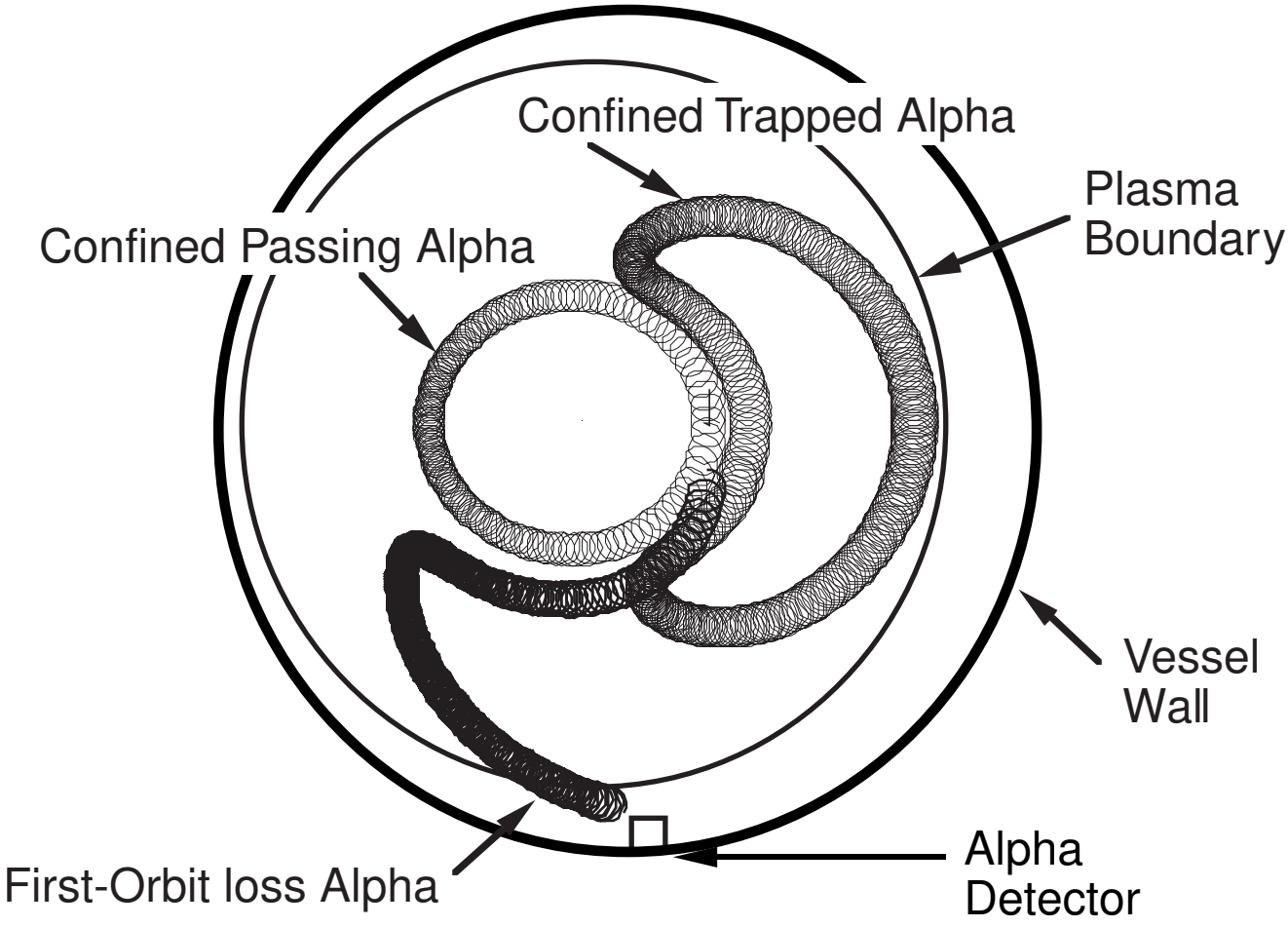

Fig. 41 Illustration of confined passing alpha particle orbits, confined trapped alpha on banana orbits and unconfined trapped alphas.

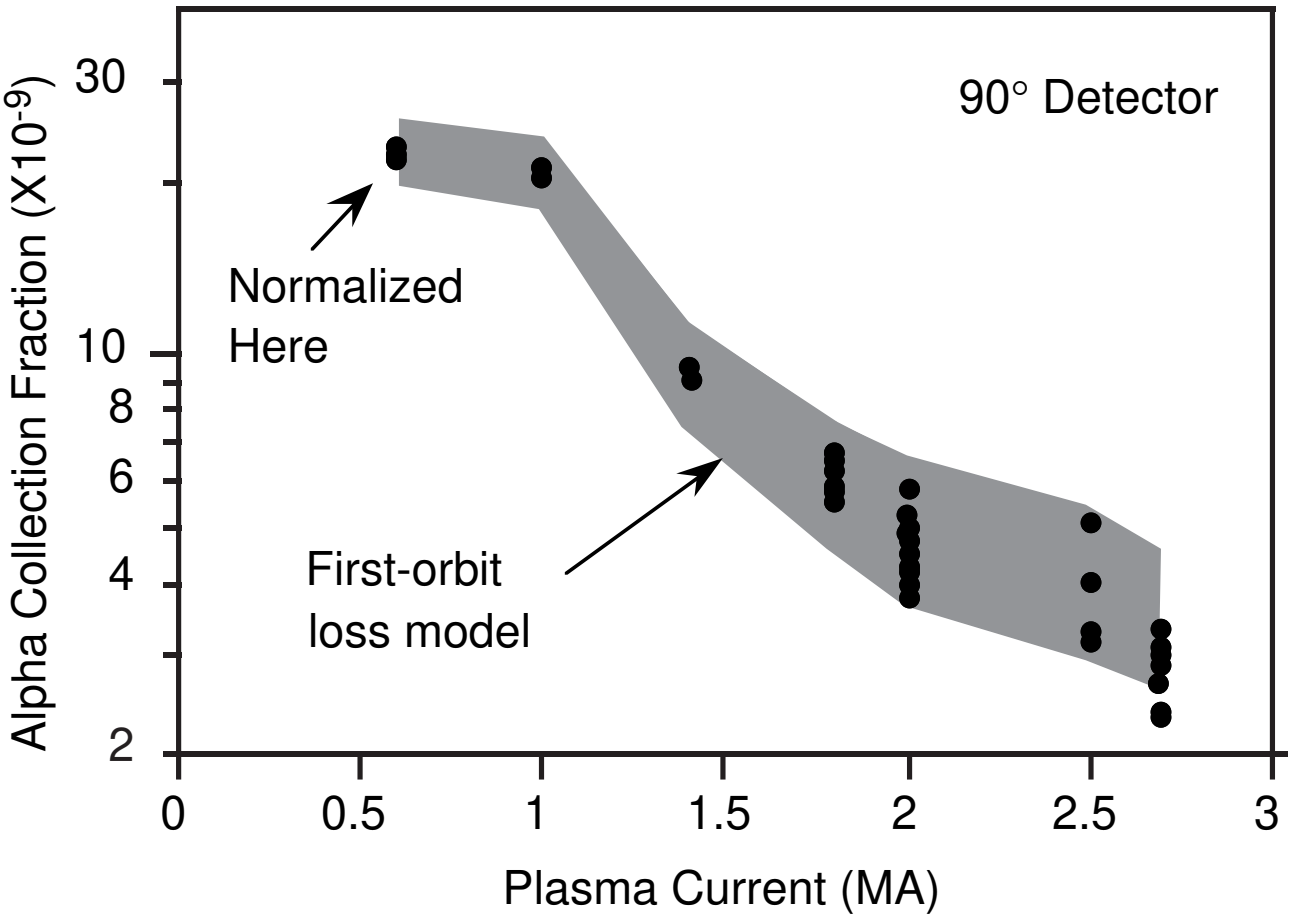

Fig. 42 Fraction of alpha particles collected by a detector located near the bottom of the vessel (90^{o}). The decrease in loss with increasing current is in good agreement with the predictions of the first orbit loss model. The data is normalized at low currents as indicated (Zweben *et al.,* 1995a).

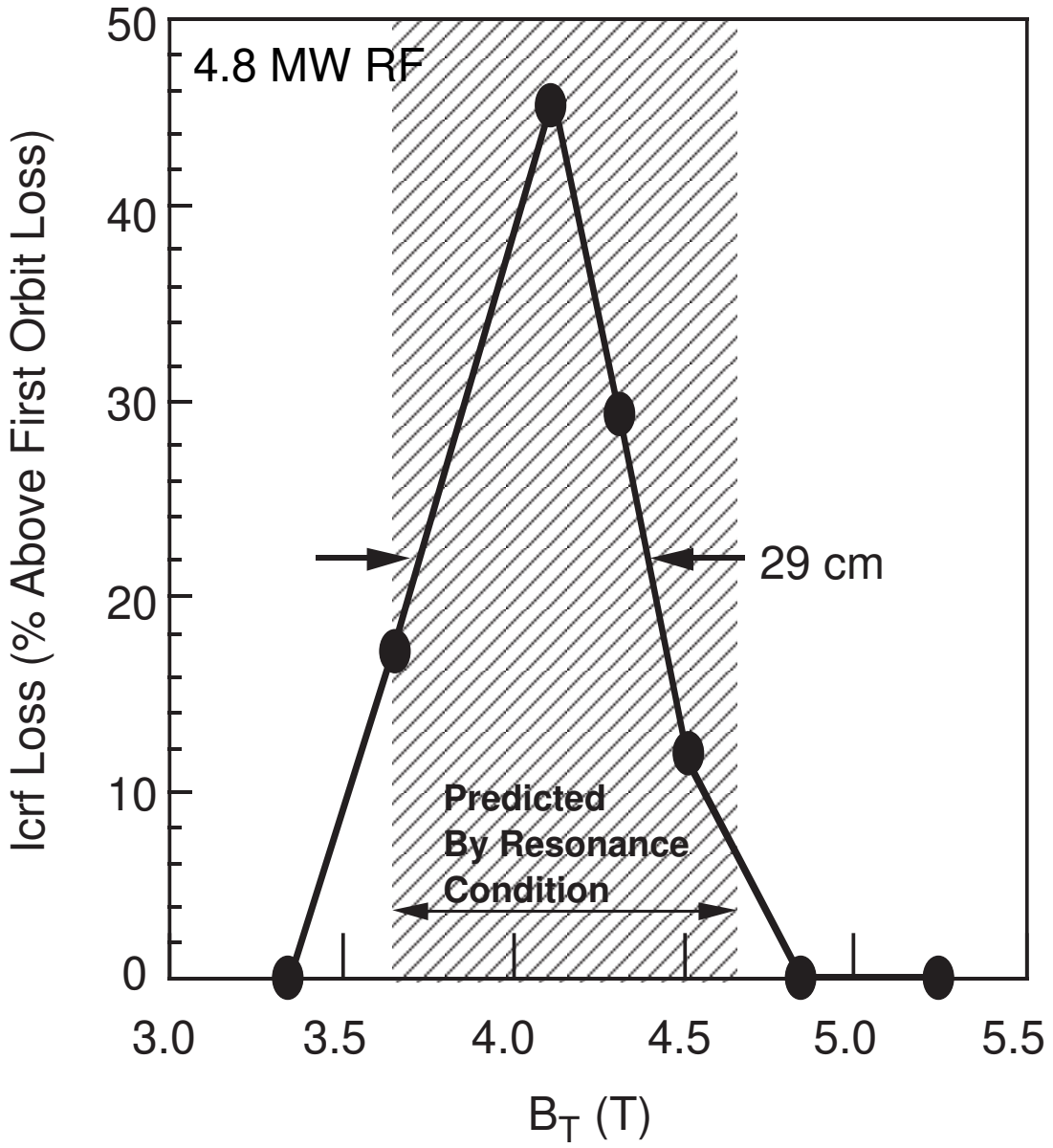

Fig. 43 The increase in alpha loss to the detector at the bottom of the machine resulting from ICRF waves is plotted as a function of toroidal field. The shaded range of toroidal field denotes where marginally passing alpha particles can be in Doppler-shifted resonance with the waves. Loss proceeds by conversion of these marginally passing orbits to lost banana orbits as the alphas are heated.

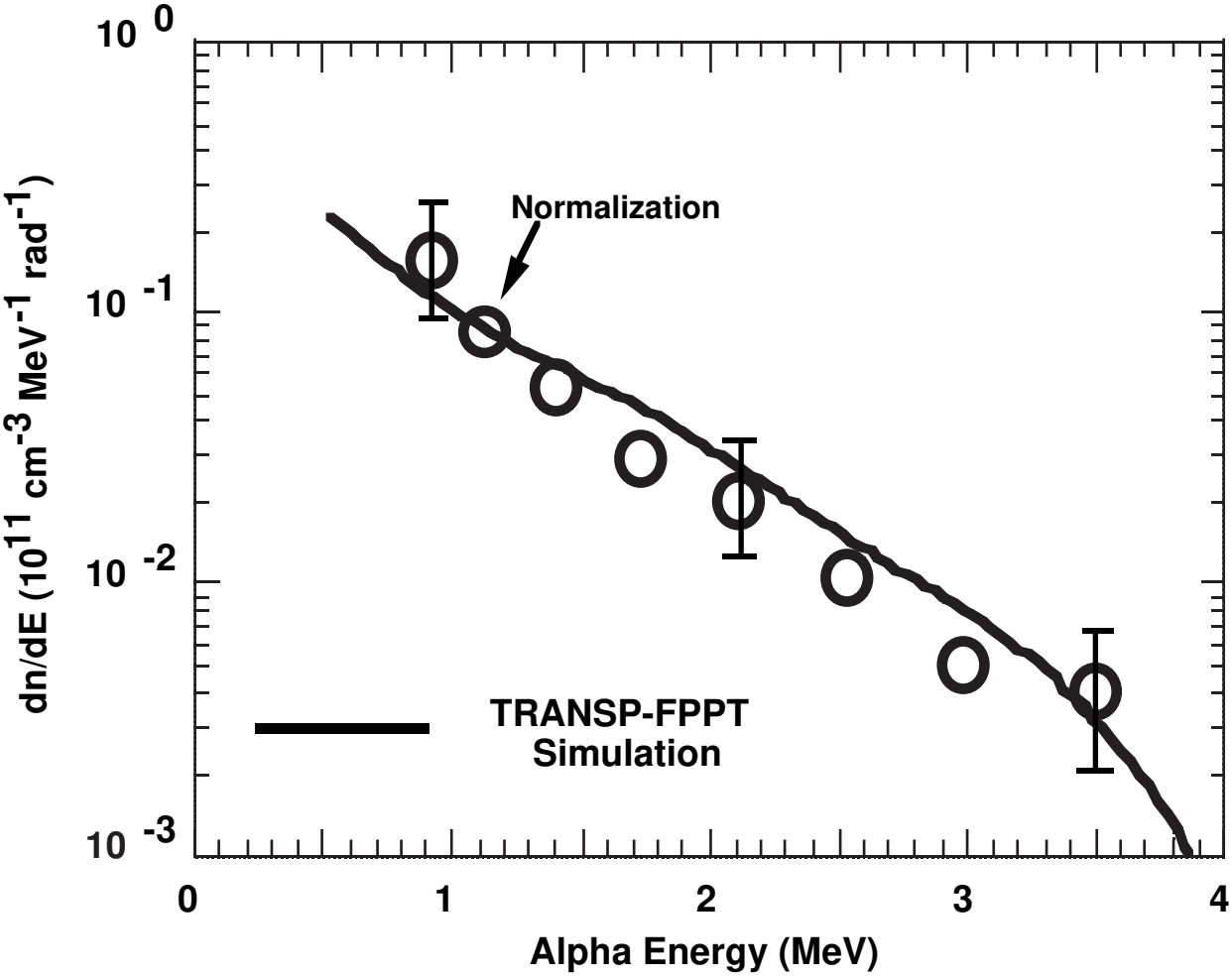

Fig. 44 Measurements of the confined alpha particle spectrum following neutral beam heating of a D-T plasma. The TRANSP calculations which are normalized at one point are in good agreement with the observed slowing down spectrum (Petrov *et al.,* 1995; Medley *et al.,* 1996a).

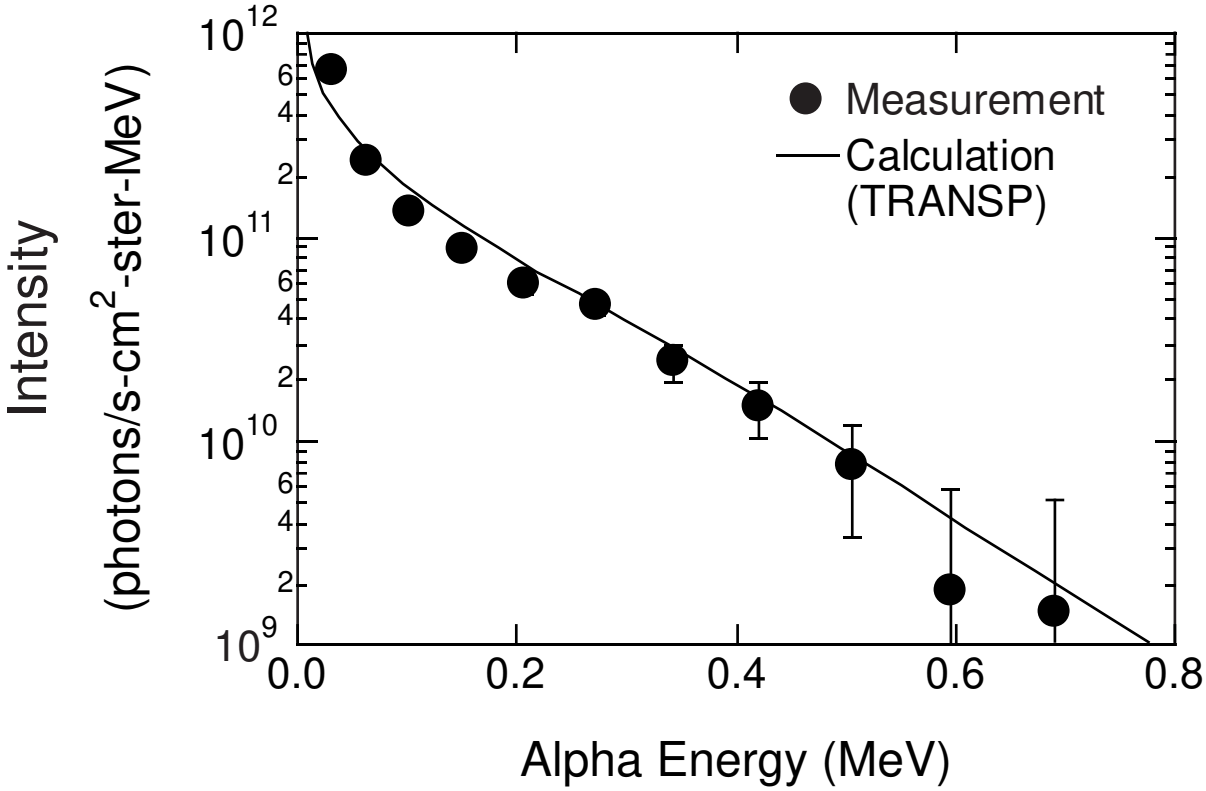

Fig. 45 Measured alpha-CHERS spectra at r/a=0.3 in a non-sawtoothing TFTR D-T supershot are in good agreement with predictions based on TRANSP calculation of the alpha density (McKee *et al.,* 1995b).

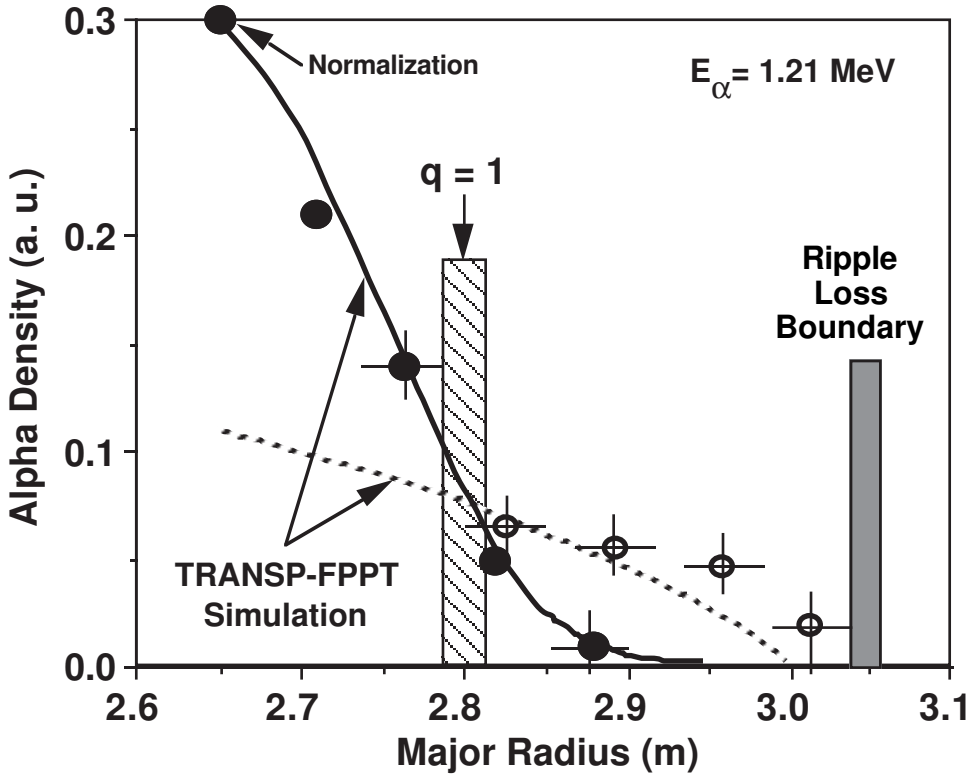

Fig. 46 Pellet charge exchange measurements of the confined alpha particles prior to and after the sawtooth instability (in a companion discharge). The observed redistribution is in reasonable accord with the magnetic reconnection model which incorporates the effect of the helical electric field (Petrov *et al.,* 1996).

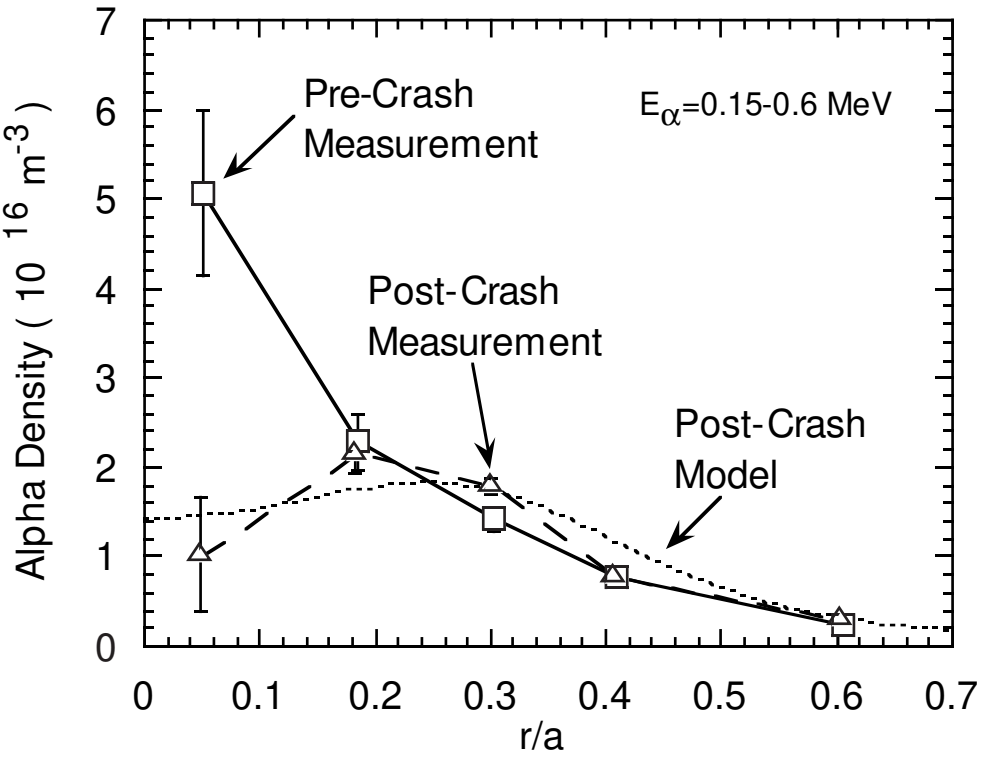

Fig. 47 Alpha-CHERS measurements of alpha density profiles before and after a sawtooth crash are in good agreement with predictions of the Kolesnichenko *et al.*, (1992) sawtooth model (Stratton *et al.,* 1996).

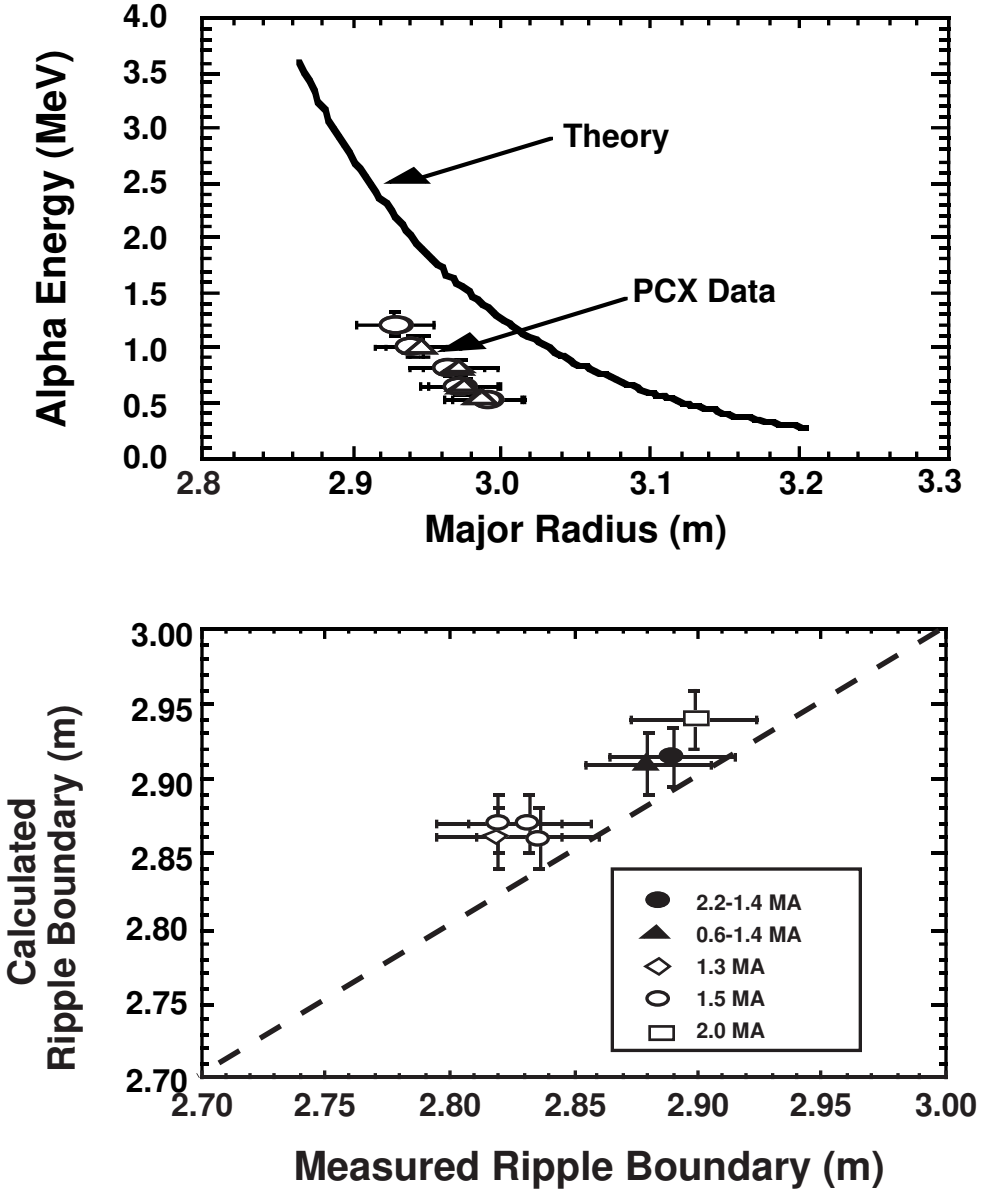

Fig. 48 The measured ripple boundary is determined from the major radius at which confined alpha particles are measured by the pellet charge exchange diagnostic. The location of the observed presence of deeply trapped alpha particles is in reasonable accord with a simple estimate of the calculated ripple boundary using the Goldston-White-Boozer formalism (Duong *et al.,* 1996a).

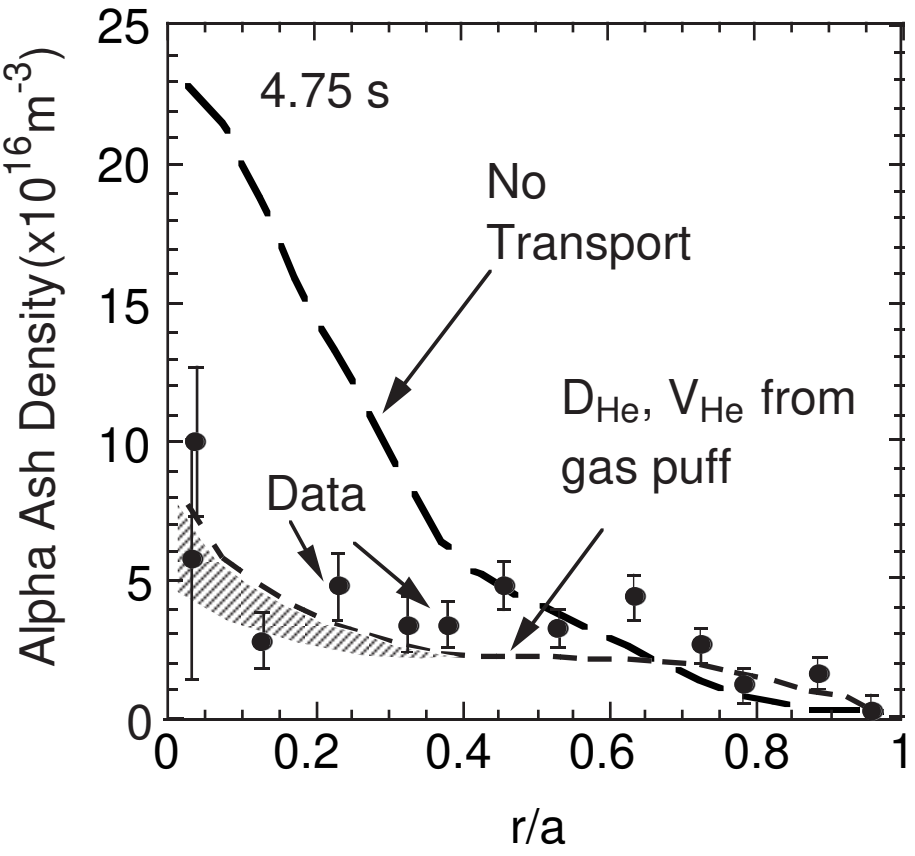

Fig. 49 Measured and modeled ash profile shapes measured 1.95 s after the start of deuterium-tritium beam injection. The errors include uncertainties related to the atomic physics of charge exchange and beam attenuation, as well as photon. The thick dashed line represents the helium ash profile shape predicted under the assumption of no radial transport of the thermalized ash. The thinner dashed line represents the predicted profile shape including the effects of radial transport and wall recycling. The shaded region is the difference in the profile shapes that are predicted with and without the central source of thermalizing alpha particles, but with transport in both cases (Synakowski *et al.,* 1995a).

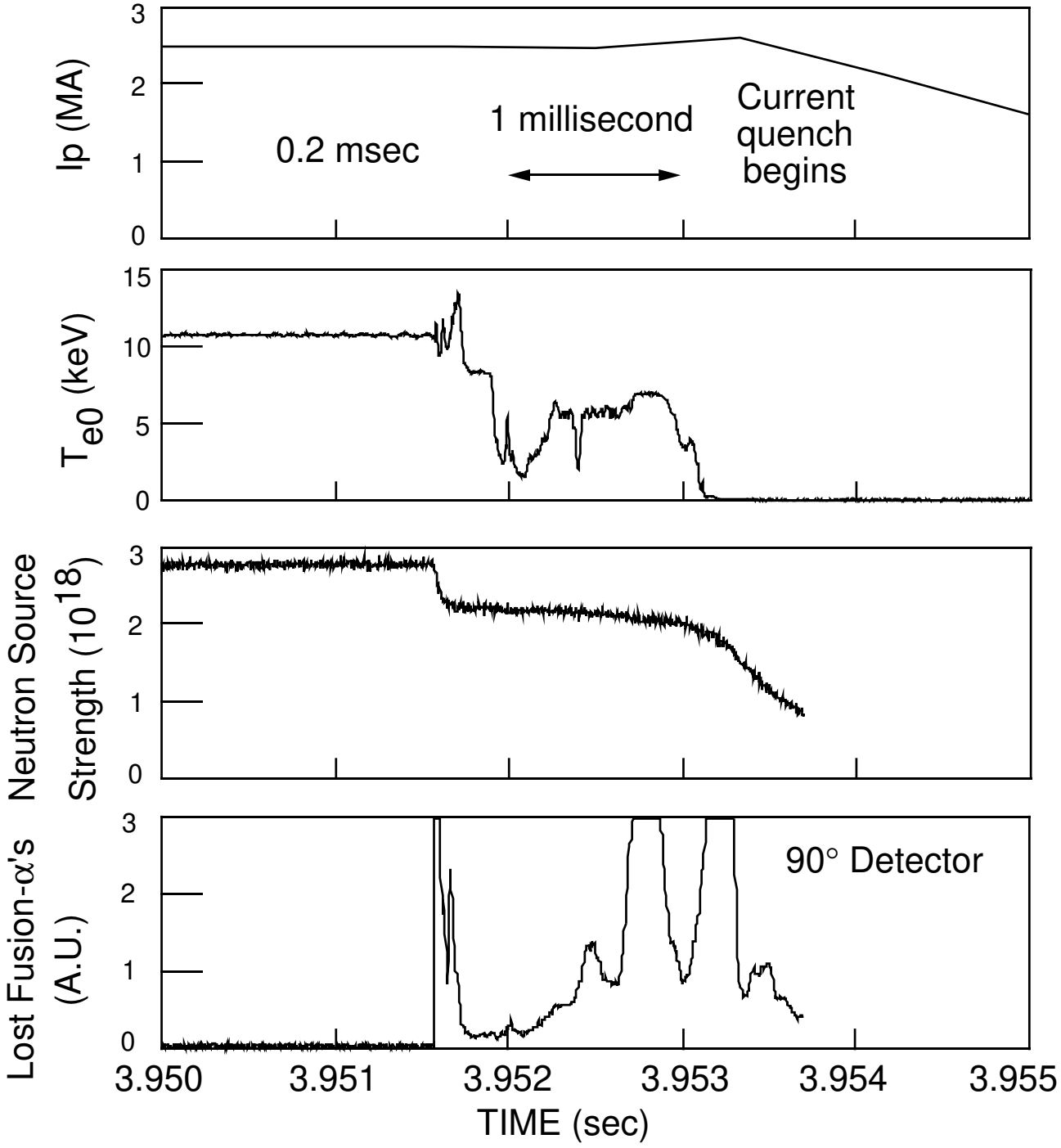

Fig. 50 The first burst of alpha particles prior at 3.9525 sec to the detector in the bottom of the vessel precedes the thermal quench of the plasma as measured by the electron temperature diagnostic and is coincident with the MHD activity responsible for the subsequent disruption (Janos *et al.,* 1996).

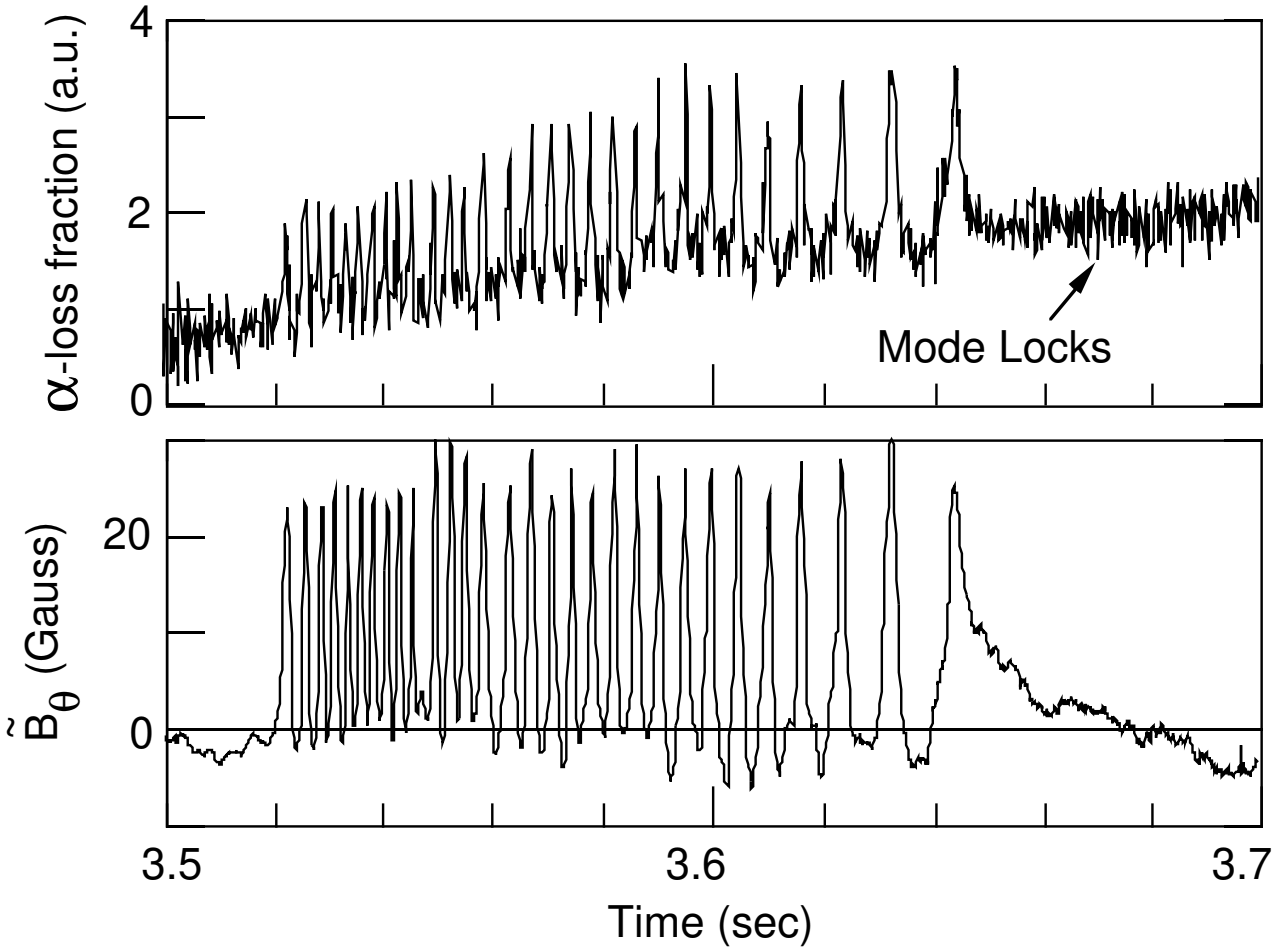

Fig. 51 Alpha particle loss due to neoclassical tearing modes correlated with fluctuations in the edge magnetic field (McGuire *et al.,* 1996).

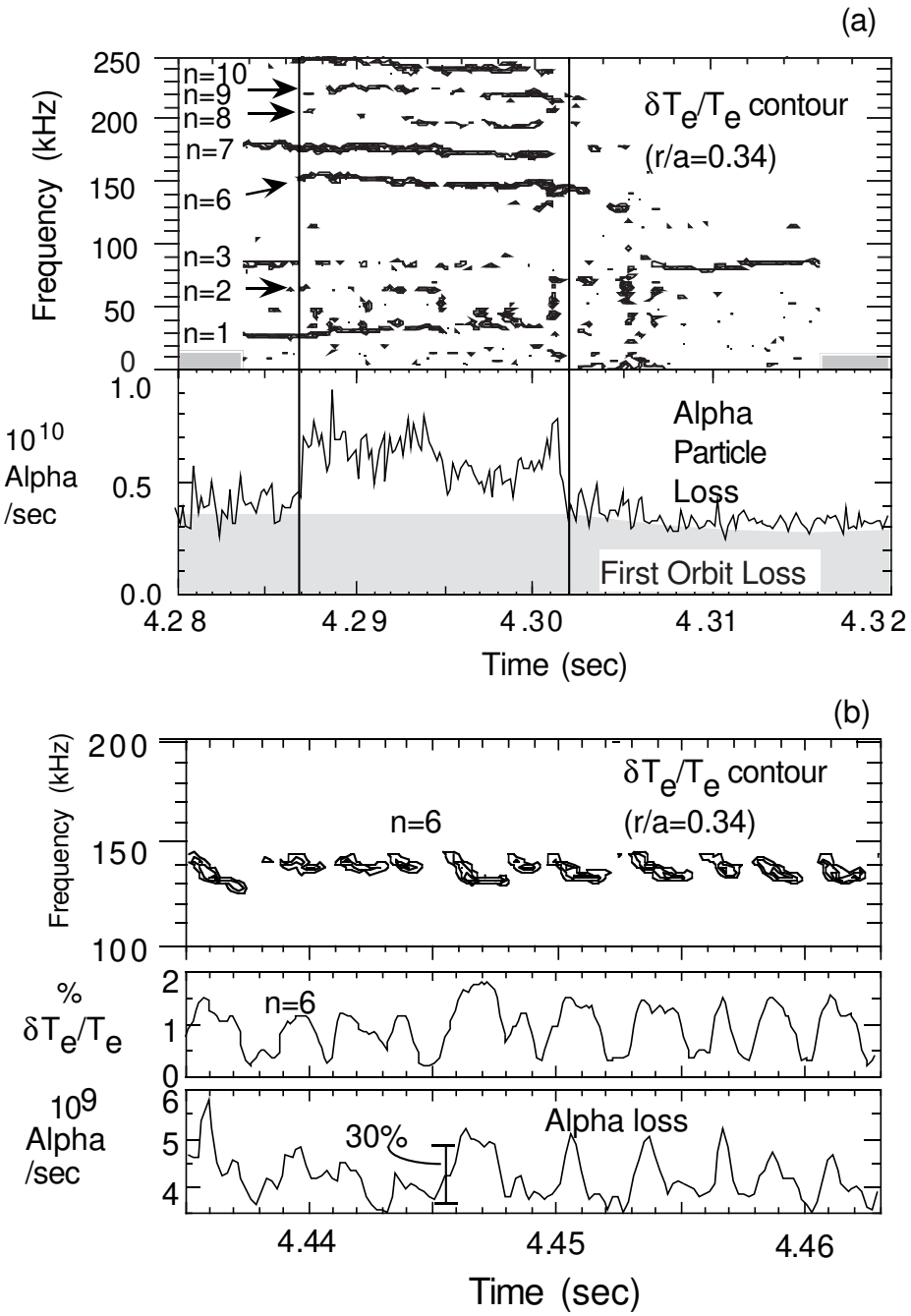

Fig. 52 Increased alpha particle loss is correlated with the occurrence of multiple high-n modes (a) as well as single n (=6) mode (b). These modes are identified as kinetic ballooning modes (KBMs) (Chang *et al.,* 1996b).

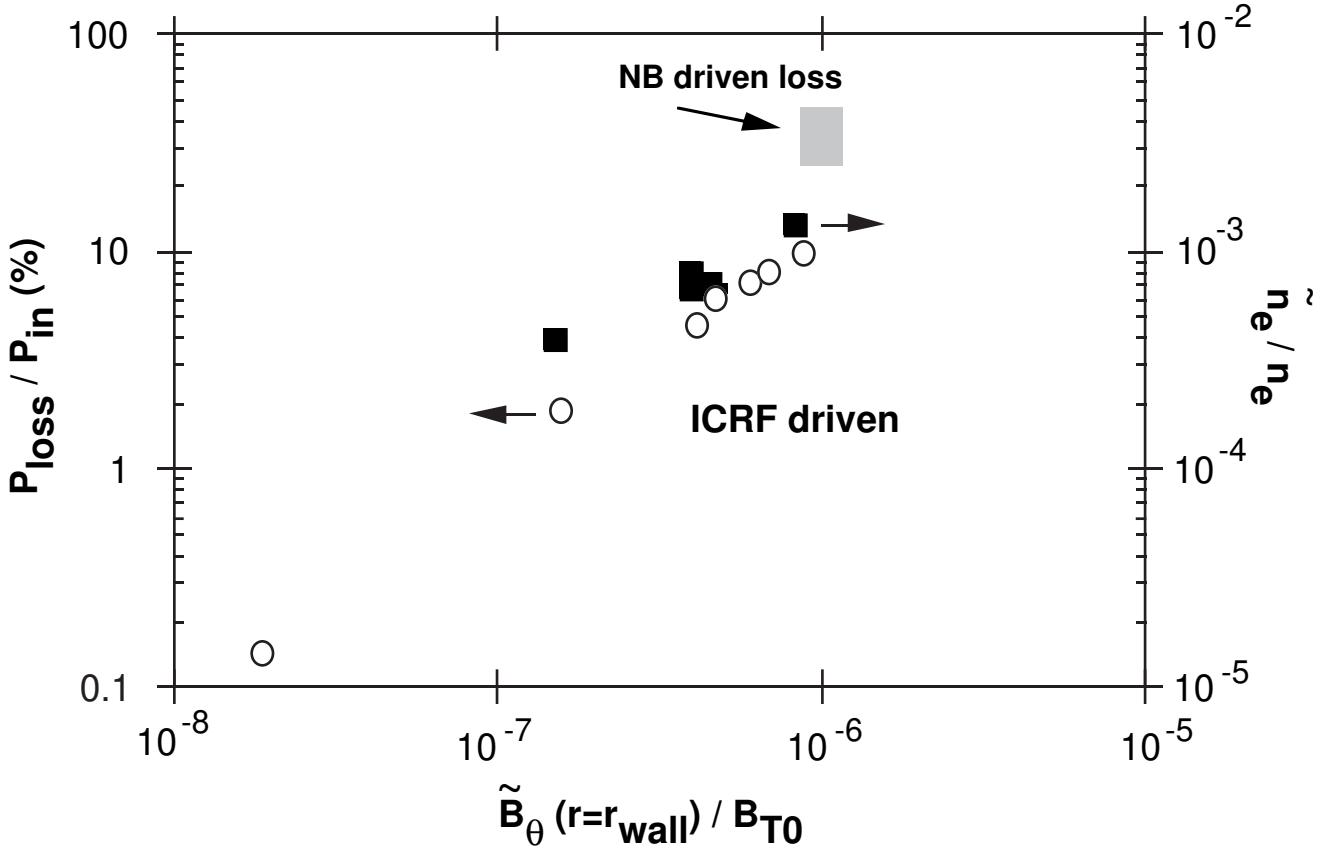

Fig. 53 Fraction of energetic particles power lost from the plasma and the TAE mode amplitude versus the heating power in TFTR discharges. Energetic particle loss resulted from TAE instabilities driven by neutral beam injection and ICRF heating but not by alpha particles (Darrow *et al.,* 1996b).

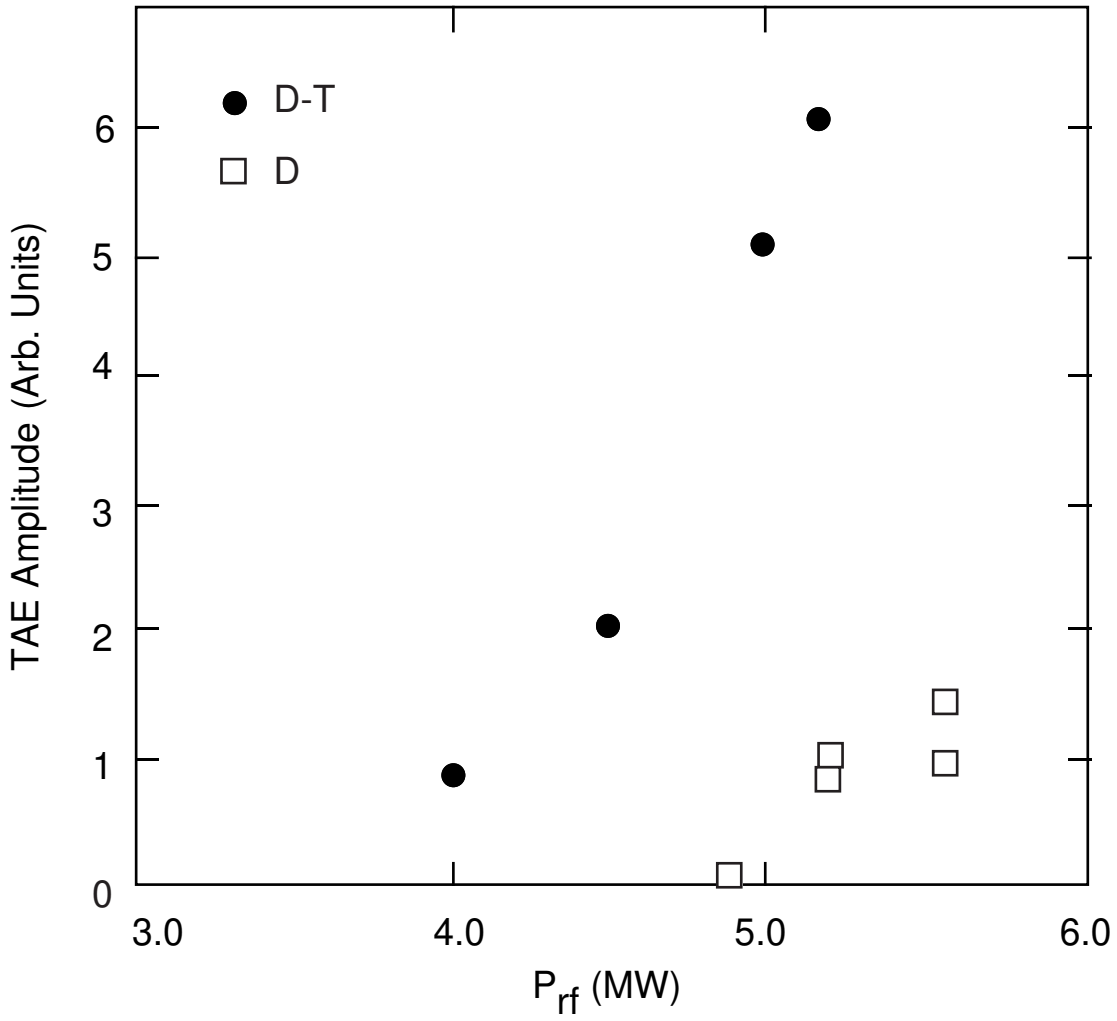

Fig. 54 TAE mode amplitude in D-T plasmas are higher than in companion D shots with the same ICRF heating power used to generate the energetic tail of H-minority particles (Wong *et al.*, 1996a).

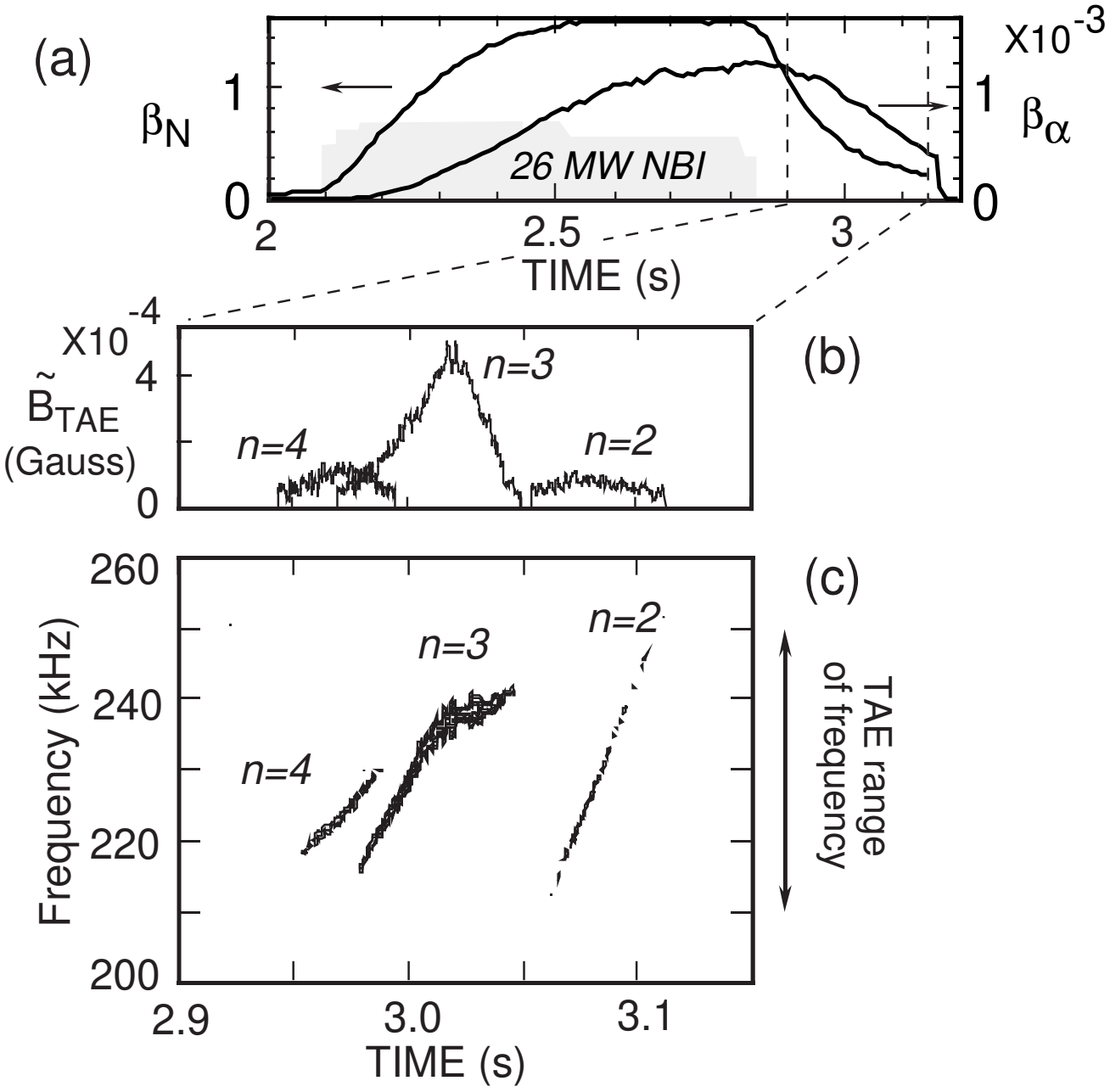

Fig. 55 Alpha-driven TAE mode in TFTR occurring ≈ 0.1s after neutral beam injection in a D-T discharge with weak central magnetic shear. a) The evolution of β_N and β_α. b) The occurrence of magnetic fluctuations with different toroidal mode numbers is observed. c) The evolution of the frequency of the magnetic fluctuations. The frequency is consistent with the density-dependent TAE frequency, and mode timing is in reasonable agreement with the theoretical prediction based on beam ion damping (Nazikian *et al.,* 1996a).

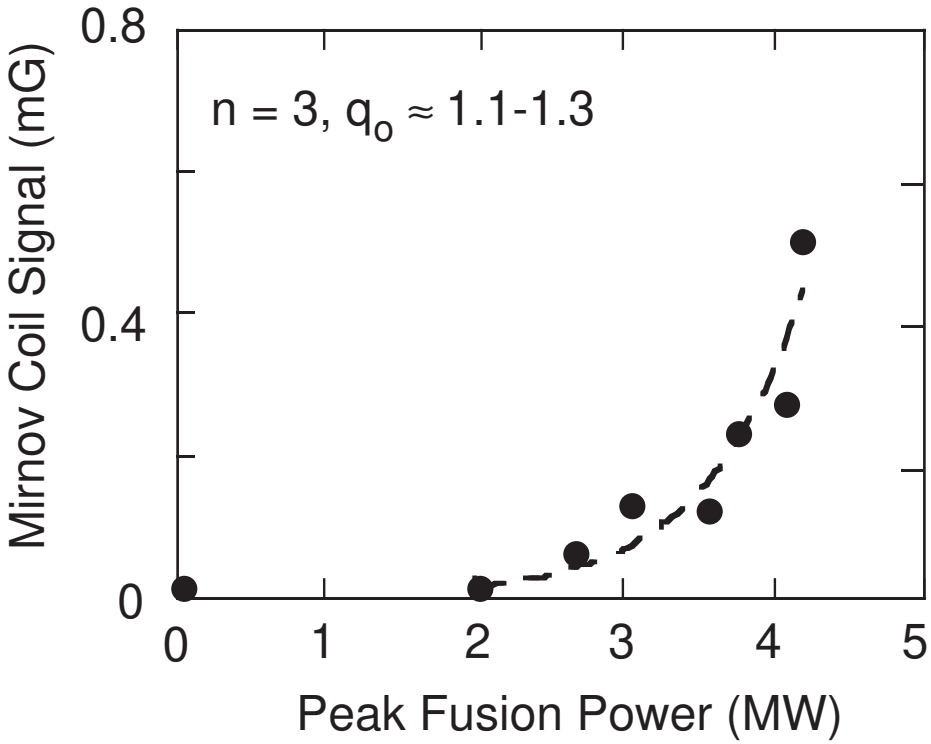

Fig. 56 TAE mode amplitude measurements using a magnetic pickup coil at the edge increases with fusion power as expected for alpha-driven TAE near threshold condition for instability. Modes are observed with $\beta_\alpha(0)$ >0.03% in weak central shear discharge with q_o ~ 1.1 - 1.3 (Nazikian *et al.,* 1996a).

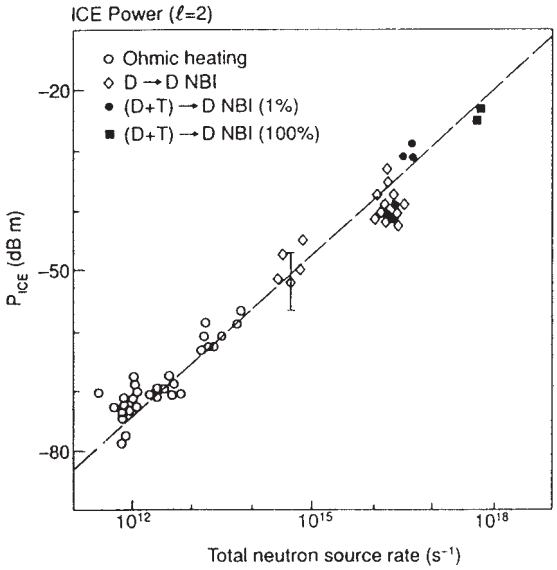

Fig. 57 Correlation between ICE intensity, P_{ICE}, and total neutral emission rate for ohmic and neutral beam heating in both D and D-T discharges (Cottrell *et al.,* 1993).

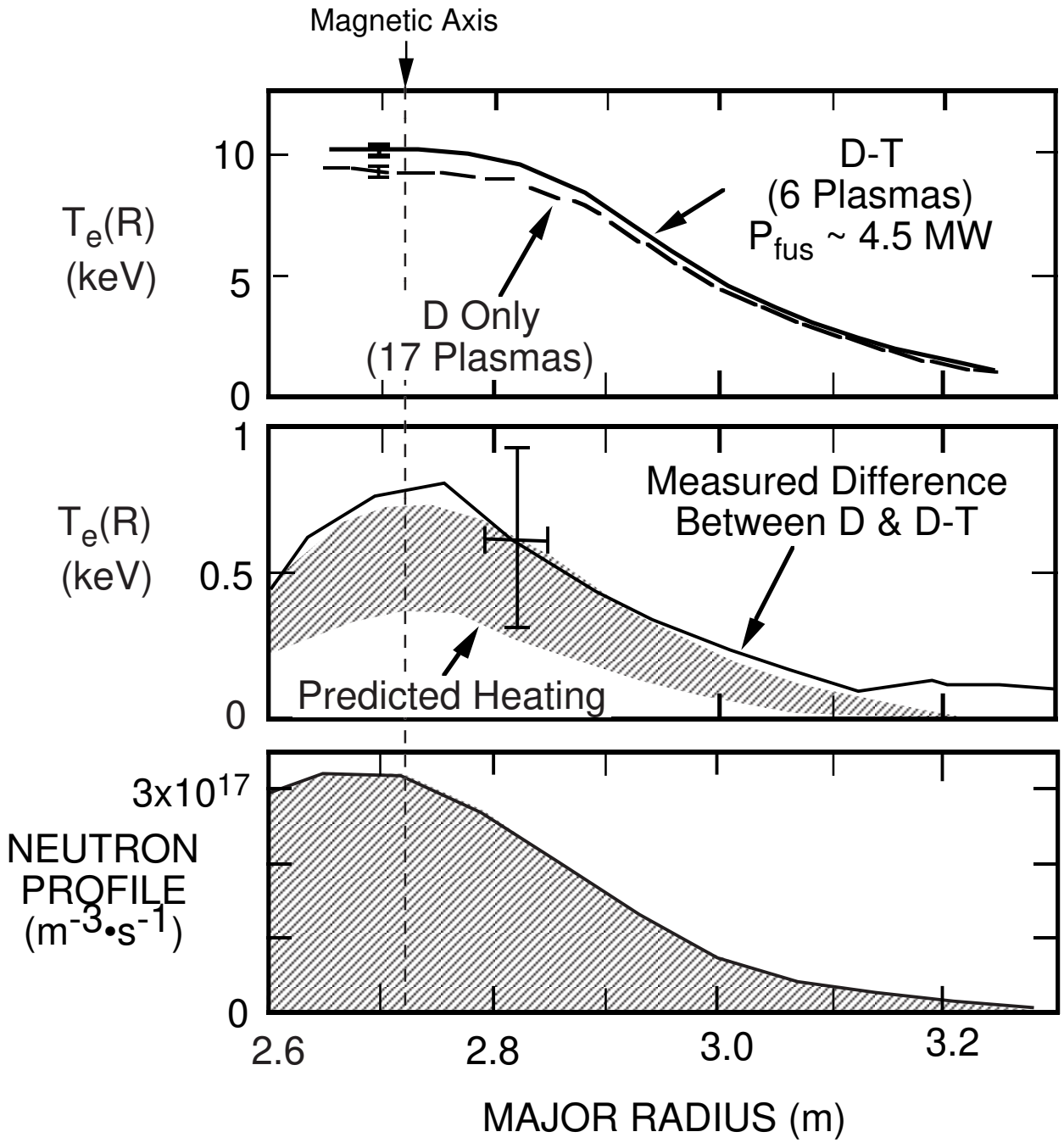

Fig. 58 Comparison of the electron temperature profile for a set of similar D-T and D discharges with comparable energy confinement times and neutral beam heating power. The measured difference in electron temperature is consistent with the predicted change due to alpha heating. The neutron profile which is a measure of the alpha particle birth profile is shown for comparison (Taylor *et al.,* 1996b).

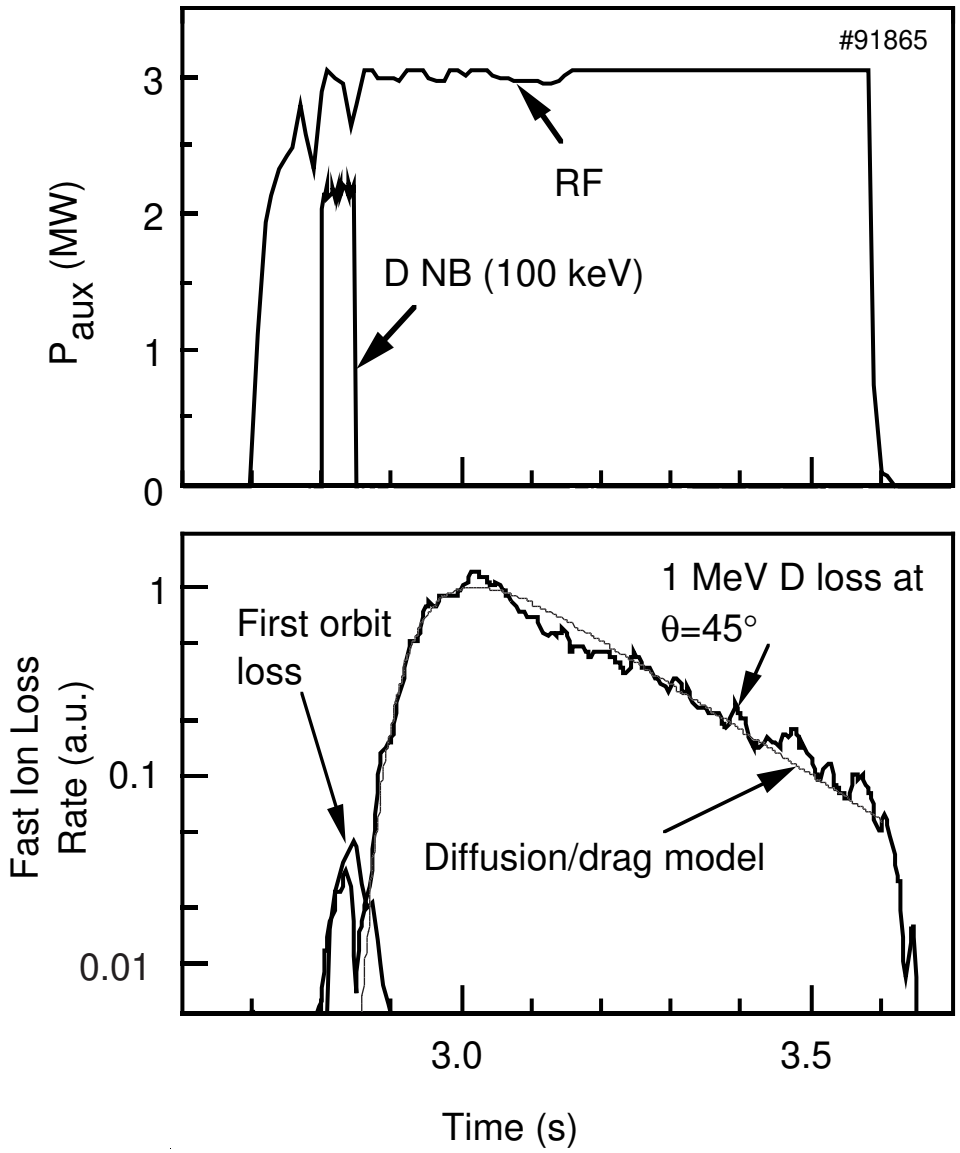

Fig. 59 Fast ion loss as measured by the 45^{o} detector in the TFTR vessel indicates the loss of deuterium beam ions heated by mode converted ion Bernstein waves. The flux of particles is in accord with a simple model of fast ion heating by the mode converted wave.

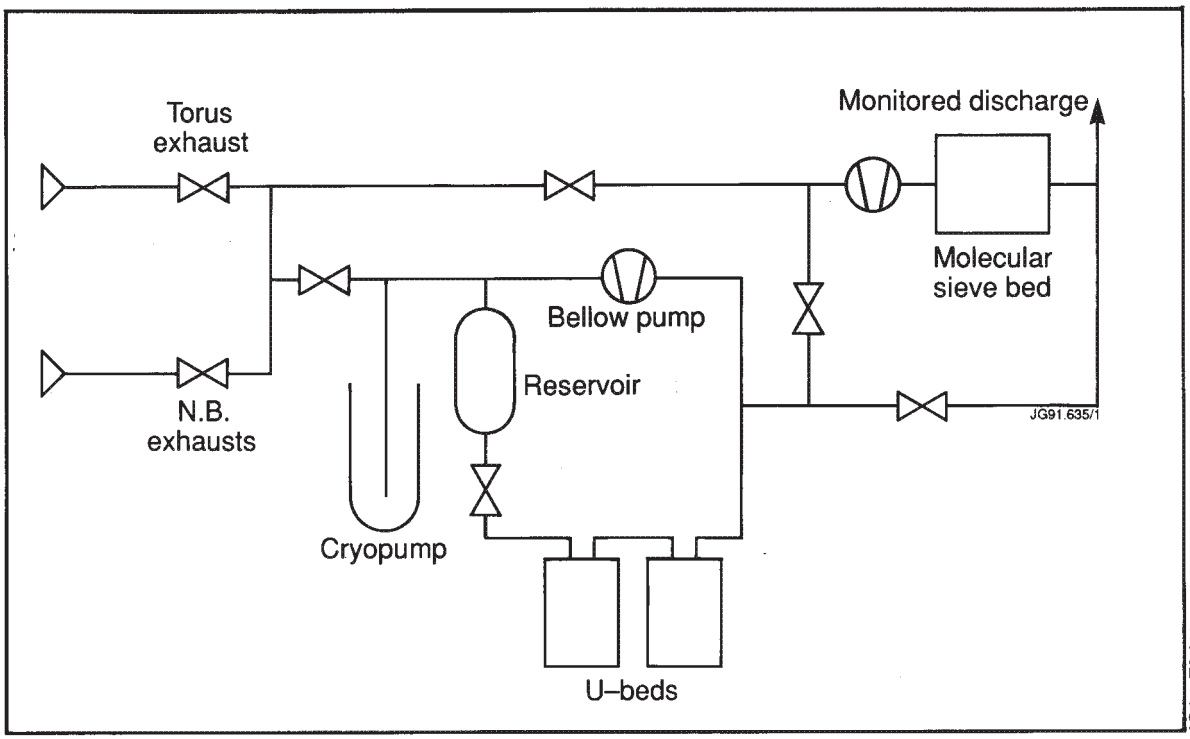

Fig. A1 The JET tritium gas collection system (JET Team, 1992).

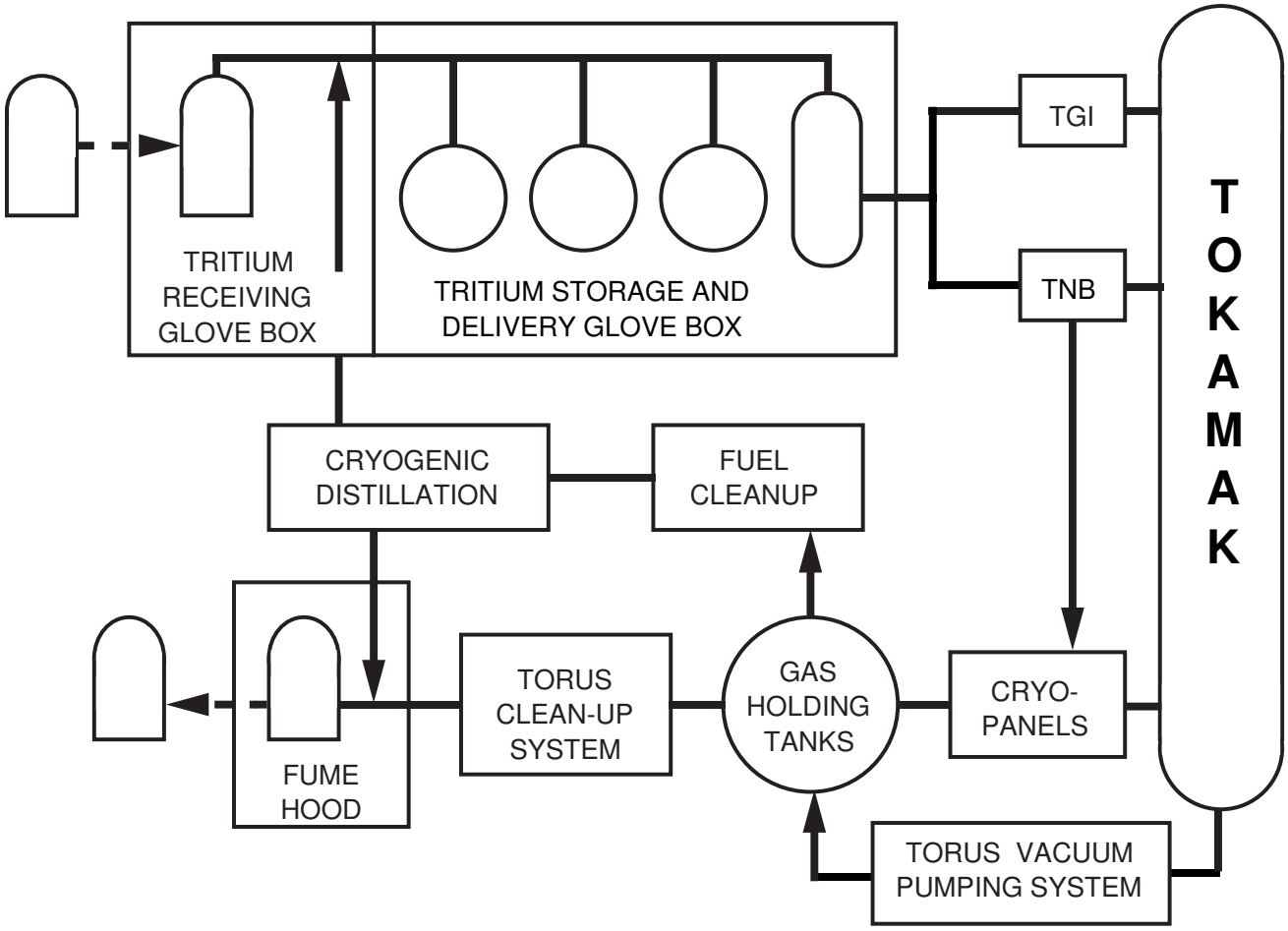

Fig. A2 The TFTR tritium gas fuel cycle (Williams *et al.,* 1996).